The Journal of Chemical Physics

RESEARCH ARTICLE | SEPTEMBER 13 2024

Kohn–Sham fragment energy decomposition analysis

Tommaso Giovannini

J. Chem. Phys. 161, 104110 (2024)
https://doi.org/10.1063/5.0216596

AIP Publishing

The Journal of Chemical Physics ARTICLE pubs.aip.org/aip/jcp

Kohn–Sham fragment energy decomposition analysis

Cite as: J. Chem. Phys. 161, 104110 (2024); doi: 10.1063/5.0216596
Submitted: 30 April 2024 • Accepted: 15 August 2024 •
Published Online: 13 September 2024

Tommaso Giovannini[a)]

AFFILIATIONS

Department of Physics, University of Rome Tor Vergata, Via della Ricerca Scientifica 1, 00133 Rome, Italy
and Scuola Normale Superiore, Piazza dei Cavalieri 7, 56126 Pisa, Italy

Note: This paper is part of the 2024 JCP Emerging Investigators Special Collection.
[a)]**Author to whom correspondence should be addressed:** tommaso.giovannini@uniroma2.it
and giovannini.tommaso@gmail.com

ABSTRACT

We introduce the concept of Kohn–Sham fragment localized molecular orbitals (KS-FLMOs), which are Kohn–Sham molecular orbitals (MOs) localized in specific fragments constituting a generic molecular system. In detail, we minimize the local electronic energies of various fragments, while maximizing the repulsion between them, resulting in the effective localization of the MOs. We use the developed KS-FLMOs to propose a novel energy decomposition analysis, which we name Kohn–Sham fragment energy decomposition analysis, which allows for rationalizing the main non-covalent interactions occurring in interacting systems both *in vacuo* and in solution, providing physical insights into non-covalent interactions. The method is validated against state-of-the-art energy decomposition analysis techniques and with high-level calculations.

I. INTRODUCTION

Understanding intermolecular interactions is fundamental for shedding light on various chemical and biological phenomena.[1] Non-covalent interactions drive various metabolic pathways and influence many physicochemical properties of materials and liquids, including their response to light.[2–6] To investigate embedded systems, most theoretical approaches rely on a chemically intuitive, hierarchical breakdown of the system under study,[5,7,8] under the assumption that the properties of interest, ranging from energetics to spectroscopy, are generally localized to specific system components, as in the case of localized electronic excitations.[9–15] To conceptualize these localized properties, localized molecular orbitals (LMOs) are often exploited,[12,16–22] serving as a conceptual bridge between chemical intuition and theoretical frameworks.[20,22–25]

In this work, we present a novel category of LMOs, specifically designed to be localized within specific fragments of molecular systems, as rooted in density functional theory (DFT) frameworks. We refer to these as Kohn–Sham fragment localized molecular orbitals (KS-FLMOs). This theory builds upon the same principles as our previously introduced FLMOs defined at the Hartree–Fock (HF)[26,27] level but translated in a KS-DFT picture. The method is based on the reformulation of the DFT energy for a system composed of multiple fragments. The local electronic KS energy of each fragment is then minimized while maintaining the total energy of the system constant. The minimization process inherently maximizes the repulsion between the fragments, thus resulting in molecular orbitals (MOs) that are substantially localized to individual fragments.[27] Our methodology adopts a top–down variational approach, which localizes canonical KS MOs through an energy-based procedure, thus differentiating from other fragment localization techniques.[28–33]

KS-FLMOs enable the calculation of local properties and energetics of interacting fragments. Here, they are exploited to introduce a novel energy decomposition analysis, which we name Kohn–Sham fragment energy decomposition analysis (KS-FEDA). The development of EDA methods has attracted much interest in the literature because decomposing the interaction energy in terms of physically consistent quantities allows for an in-depth investigation and rationalization of the dominant contributions regulating many chemical and biological phenomena.[12,34–46] EDA methods can be categorized into variational-,[17,40,47–55] perturbation-,[56–59] or real-space-based[60–62] approaches. Varia-

tional methods have been pioneered by Kitaura–Morokuma-EDA (KM-EDA),[47] which decomposes the interaction energy at the HF level, by considering electrostatic, exchange, polarization, charge-transfer, and mixed terms. Many EDA techniques belong to this group, differing in how the self-consistent energy components are determined. Led by symmetry-adapted perturbation theory (SAPT),[57,58,63] perturbation methods analyze intermolecular interactions using perturbation theory, under the assumption of their small magnitude. Real-space methods partition the physical space into domains based on interacting electron densities.[62] Similar to KS-FEDA, some EDA techniques, such as the local energy decomposition (LED)[41,64–67] and LMO-EDA[36,68–70] methods, exploit localized MOs to decompose the interaction energy. LED is based on the DLPNO approach for CCSD(T) and permits the decomposition of the entire interaction energy, by localizing the MOs with standard procedures (such as Boys[20] or Pipek–Mezey[21]) and assigning them to the interacting fragments. LMO-EDA is a method merging variational EDA with perturbation theory, adaptable to both HF and KS localized orbitals.[36]

KS-FEDA decomposes the self-consistent DFT energy by first localizing the MOs on the specific fragments by means of the KS-FLMOs procedure. The interaction energy is dissected in terms of electrostatics, exchange, correlation, and electronic-preparation energies, the latter accounting for the energy spent to bring the monomers into the final electronic configuration of the supermolecule. Dispersion energy is also accounted for by resorting to the charge-dependent London-dispersion correction D4 model;[71–73] however, the method is general and can be coupled to more sophisticated dispersion approaches, such as Tkatchenko–Scheffler,[74] many-body dispersion,[75] non-local functionals, or double hybrids.[76,77] The KS-FEDA partition is conceptually similar to that proposed in the LED technique (at the SCF level),[64] but defined in a KS-DFT formalism. For this reason, we label this novel EDA KS-FEDA(LED). The KS-FEDA energy decomposition is performed by using KS-FLMOs, which are orthogonal by definition.[27] This is similar to other energy decompositions (e.g., LED) but differs from most EDA techniques, in which the MOs belonging to different fragments are generally non-orthogonal. This implies that the interactions are computed with relaxed, distorted molecular densities.[38] This is also similar to absolutely localized MO-EDA.[17,38,78–80] As a consequence, the multipoles that reproduce the electrostatic interaction vary as a function of the intermolecular distance. To properly compare our approach to conventional EDA methods, we thus introduce a further partitioning of the KS-FEDA(LED) energetic terms by introducing frozen (derived from the monomers' undistorted densities) and induced energy contributions, which are divided into two parts: one arising from imposing the proper antisymmetry of the total wave function and one arising from the self-consistent orbital relaxation. The resulting partitioning defines the KS-FEDA technique. KS-FEDA energetic contributions can be directly compared to conventional EDA techniques, also offering the possibility of investigating the effects of antisymmetry on each energetic component. Similar to other EDAs, such as extended transition state combined with natural orbitals for chemical valence (ETS-NOCV)-based approaches,[81,82] KS-FEDA allows the dissection of the interaction energy into meaningful components representing different steps toward the dimer formation from the isolated fragments.

Finally, we extend the KS-FLMO procedure and the related KS-FEDA method to study non-covalent interactions of molecular systems in solution, by exploiting the polarizable continuum model (PCM)[83–85] in its integral equation formalism (IEF).[86] In KS-FEDA, the solvent modifies the density and the KS-FLMOs of monomers, thus indirectly affecting all the energetic components, as well as providing an explicit solvation term due to mutual solute–solvent polarization.

The paper is structured as follows: first, the KS-FLMOs theory is developed for a generic hybrid functional, followed by the derivation of the KS-FEDA technique both *in vacuo* and in solution. Following this, we briefly summarize the computational details, and we evaluate the novel KS-FEDA scheme on widely exploited datasets for non-covalent interactions, such as A24,[87] S22,[88] and IHB15.[89] Conclusions and future perspectives end the manuscript.

II. THEORETICAL MODEL

A. Kohn–Sham fragment localized molecular orbitals

The DFT energy of a molecular system for a generic DFT functional reads

$$E[\mathbf{D}] = \mathrm{Tr}\,\mathbf{hD} + \frac{1}{2}\mathrm{Tr}\,\mathbf{DJ(D)} - \frac{1}{2}c_x\,\mathrm{Tr}\,\mathbf{DK(D)} + (1-c_x)E_x[\mathbf{D}] + E_c[\mathbf{D}], \tag{1a}$$

$$= \mathrm{Tr}\,\mathbf{hD} + \frac{1}{2}\mathrm{Tr}\,\mathbf{DJ(D)} - \frac{1}{2}\mathrm{Tr}\,\mathbf{DK(D)} + (1-c_x)(E_x[\mathbf{D}] - E^{HF,x}[\mathbf{D}]) + E_c[\mathbf{D}], \tag{1b}$$

where $\mathbf{h}$, $\mathbf{J}$, and $\mathbf{K}$ are the one-electron, Coulomb, and exchange matrices, respectively. $\mathbf{D}$ is the one-particle density matrix expressed in the atomic orbitals (AO) basis $\{\chi_\mu\}$, while $\rho(\mathbf{r})$ is the DFT density function. The DFT functional is specified by E_x and E_c exchange and correlation energy functionals, while $E^{HFx}[\mathbf{D}]$ is the exact HF exchange. The coefficient c_x defines whether pure DFT ($c_x = 0$) or hybrid DFT functionals ($c_x \neq 0$) are used. It should be noted that Eq. (1b) is well-defined in a generalized Kohn–Sham (GKS) formalism,[90,91] which is flexible enough to account for nonlocal functionals, including hybrid, double hybrid, and range-separated types.[91] The $E_x[\mathbf{D}]$ and $E_c[\mathbf{D}]$ energies introduced in Eq. (1) can be written as

$$(1-c_x)E_x[\mathbf{D}] = (1-c_x)\int \rho(\mathbf{r})\varepsilon_x(\rho(\mathbf{r}))\mathrm{d}\mathbf{r} - \frac{\beta}{2}\mathrm{Tr}\,\mathbf{DK}^{\mathrm{LR}}(\mathbf{D}), \tag{2a}$$

$$E_c[\mathbf{D}] = \int \rho(\mathbf{r})\varepsilon_c(\rho(\mathbf{r}))\mathrm{d}\mathbf{r}, \tag{2b}$$

where ε_x and ε_c are the exchange energy densities per unit particle, respectively. $\mathbf{K}^{LR}$ accounts for DFT long-range (LR) correction in terms of the HF exchange integral using the $\mathrm{erf}(\omega r_{ij})/r_{ij}$ operator. β and ω parameters define the specific range-separated functional.[92–94] The correlation energy functional is generally written in terms of the correlation energy density per unit particle

ε_c, however, for double-hybrids and non-local functionals, can also account for MP2 and non-local corrections.[76,77] The present approach is general enough to consider such energy terms, but will not be explicitly considered in the following derivation. By considering Eq. (2), we can rewrite the total energy defined in Eq. (1a) as

$$\begin{aligned} E[\mathbf{D}] &= \mathrm{Tr}\,\mathbf{hD} + \frac{1}{2}\mathrm{Tr}\,\mathbf{DJ}(\mathbf{D}) - \frac{1}{2}c_x\,\mathrm{Tr}\,\mathbf{DK}(\mathbf{D}) \\ &\quad + (1-c_x)\int \rho(\mathbf{r})\varepsilon_x(\rho(\mathbf{r}))\mathrm{d}\mathbf{r} - \frac{\beta}{2}\mathrm{Tr}\,\mathbf{DK}^{\mathrm{LR}}(\mathbf{D}) \\ &\quad + \int \rho(\mathbf{r})\varepsilon_c(\rho(\mathbf{r}))\mathrm{d}\mathbf{r} \\ &= \mathrm{Tr}\,\mathbf{hD} + \frac{1}{2}\mathrm{Tr}\,\mathbf{DJ}(\mathbf{D}) - \frac{1}{2}c_x\,\mathrm{Tr}\,\mathbf{DK}(\mathbf{D}) \\ &\quad + \int \rho(\mathbf{r})\varepsilon_{xc}(\rho(\mathbf{r}))\mathrm{d}\mathbf{r} - \frac{\beta}{2}\mathrm{Tr}\,\mathbf{DK}^{\mathrm{LR}}(\mathbf{D}), \end{aligned} \tag{3}$$

where the exchange and correlation energy functionals per unit particle are collected in ε_{xc}. Let us now consider a system that can be decomposed into two closed-shell fragments A and B, e.g., two non-covalently interacting molecules. Such a fragment partitioning can be obtained by decomposing the density matrix of the whole system $\mathbf{D}$ into the density matrices of the two fragments ($\mathbf{D}^A$ and $\mathbf{D}^B$), reflected into an equivalent decomposition on the density functions $\rho(\mathbf{r})$,

$$\mathbf{D} = \mathbf{D}^A + \mathbf{D}^B \qquad \Rightarrow \qquad \rho(\mathbf{r}) = \rho^A(\mathbf{r}) + \rho^B(\mathbf{r}). \tag{4}$$

The decomposition in Eq. (4) can be performed using different methods. In this work, we use a partial Cholesky decomposition of the total density matrix for the A and B occupied molecular orbitals (MOs), from which the density matrices $\mathbf{D}^A$ and $\mathbf{D}^B$ are calculated (*vide infra*).[26,95–98] In this way, we ensure that A and B MOs remain orthogonal in the subsequent SCF procedures.[99]

Equation (3) can be rewritten by using the partition in Eq. (4),[100,101]

$$\begin{aligned} E &= \mathrm{Tr}\,\mathbf{hD}^A + \frac{1}{2}\mathrm{Tr}\,\mathbf{D}^A\mathbf{J}(\mathbf{D}^A) - \frac{1}{2}c_x\,\mathrm{Tr}\,\mathbf{D}^A\mathbf{K}(\mathbf{D}^A) \\ &\quad + \int \rho^A(\mathbf{r})\varepsilon_{xc}(\rho^A(\mathbf{r}))\mathrm{d}\mathbf{r} - \frac{\beta}{2}\mathrm{Tr}\,\mathbf{D}^A\mathbf{K}^{\mathrm{LR}}(\mathbf{D}^A) \\ &\quad + \mathrm{Tr}\,\mathbf{hD}^B + \frac{1}{2}\mathrm{Tr}\,\mathbf{D}^B\mathbf{J}(\mathbf{D}^B) - \frac{1}{2}c_x\,\mathrm{Tr}\,\mathbf{D}^B\mathbf{K}(\mathbf{D}^B) \\ &\quad + \int \rho^B(\mathbf{r})\varepsilon_{xc}(\rho^B(\mathbf{r}))\mathrm{d}\mathbf{r} - \frac{\beta}{2}\mathrm{Tr}\,\mathbf{D}^B\mathbf{K}^{\mathrm{LR}}(\mathbf{D}^B) \\ &\quad + \int \rho^A(\mathbf{r})\varepsilon_{xc}(\rho^B(\mathbf{r}))\mathrm{d}\mathbf{r} + \int \rho^B(\mathbf{r})\varepsilon_{xc}(\rho^A(\mathbf{r}))\mathrm{d}\mathbf{r} \\ &\quad + \mathrm{Tr}\,\mathbf{D}^A\mathbf{J}(\mathbf{D}^B) - c_x\,\mathrm{Tr}\,\mathbf{D}^A\mathbf{K}(\mathbf{D}^B) - \beta\,\mathrm{Tr}\,\mathbf{D}^A\mathbf{K}^{\mathrm{LR}}(\mathbf{D}^B) \\ &\quad + E^{AB}_{\mathrm{non-add}} + h_{nuc}. \end{aligned} \tag{5}$$

The last term $E^{AB}_{\mathrm{non-add}}$ originates from the non-linearity of ε_x and ε_c energy functionals per unit particle, and it is defined as[100]

$$\begin{aligned} E^{AB}_{\mathrm{non-add}} &= \int \rho(\mathbf{r})\varepsilon_{xc}(\rho(\mathbf{r}))\mathrm{d}\mathbf{r} - \int \rho(\mathbf{r})\varepsilon_{xc}(\rho^A(\mathbf{r}))\mathrm{d}\mathbf{r} \\ &\quad - \int \rho(\mathbf{r})\varepsilon_{xc}(\rho^B(\mathbf{r}))\mathrm{d}\mathbf{r}. \end{aligned} \tag{6}$$

As can be seen from Eq. (5), the energy of the total system is formally equivalent to the DFT energy if the decomposed density $\mathbf{D}$ corresponds to the fully converged DFT density.

Equation (5) can be partitioned into three terms, the energy of the fragments and their interaction energy, by separating the one-electron terms into the kinetic $\mathbf{T}$ and electron–nuclear interaction $\mathbf{V}_A$ and $\mathbf{V}_B$ with the A and B nuclei, respectively. Such three energy contributions read

$$E = E^A_{(AB)} + E^B_{(AB)} + E^{AB}_{int,(AB)}, \tag{7a}$$

$$\begin{aligned} E^A_{(AB)} &= \mathrm{Tr}\,\mathbf{h}^A\mathbf{D}^A + \frac{1}{2}\mathrm{Tr}\,\mathbf{D}^A\mathbf{J}(\mathbf{D}^A) - \frac{1}{2}c_x\,\mathrm{Tr}\,\mathbf{D}^A\mathbf{K}(\mathbf{D}^A) \\ &\quad + \int \rho^A(\mathbf{r})\varepsilon_{xc}(\rho^A(\mathbf{r}))\mathrm{d}\mathbf{r} - \frac{\beta}{2}\mathrm{Tr}\,\mathbf{D}^A\mathbf{K}^{\mathrm{LR}}(\mathbf{D}^A) + h^A_{nuc}, \end{aligned} \tag{7b}$$

$$\begin{aligned} E^B_{(AB)} &= \mathrm{Tr}\,\mathbf{h}^B\mathbf{D}^B + \frac{1}{2}\mathrm{Tr}\,\mathbf{D}^B\mathbf{J}(\mathbf{D}^B) - \frac{1}{2}c_x\,\mathrm{Tr}\,\mathbf{D}^B\mathbf{K}(\mathbf{D}^B) \\ &\quad + \int \rho^B(\mathbf{r})\varepsilon_{xc}(\rho^B(\mathbf{r}))\mathrm{d}\mathbf{r} - \frac{\beta}{2}\mathrm{Tr}\,\mathbf{D}^B\mathbf{K}^{\mathrm{LR}}(\mathbf{D}^B) + h^B_{nuc}, \end{aligned} \tag{7c}$$

$$\begin{aligned} E^{AB}_{int,(AB)} &= \mathrm{Tr}\,\mathbf{V}^A\mathbf{D}^B + \mathrm{Tr}\,\mathbf{V}^B\mathbf{D}^A + \mathrm{Tr}\,\mathbf{D}^A\mathbf{J}(\mathbf{D}^B) \\ &\quad - c_x\,\mathrm{Tr}\,\mathbf{D}^A\mathbf{K}(\mathbf{D}^B) - \beta\,\mathrm{Tr}\,\mathbf{D}^A\mathbf{K}^{\mathrm{LR}}(\mathbf{D}^B) \\ &\quad + \int \rho^A(\mathbf{r})\varepsilon_{xc}(\rho^B(\mathbf{r}))\mathrm{d}\mathbf{r} + \int \rho^B(\mathbf{r})\varepsilon_{xc}(\rho^A(\mathbf{r}))\mathrm{d}\mathbf{r} \\ &\quad + E^{AB}_{\mathrm{non-add}} + h^{AB}_{nuc}, \end{aligned} \tag{7d}$$

where h^A_{nuc} and h^B_{nuc} are the nuclear repulsion of the A and B fragments, respectively, while h^{AB}_{nuc} is the nuclear repulsion between the A and B nuclei. In Eqs. (7b) and (7c), we have introduced the fragment one-electron Hamiltonian $\mathbf{h}^X = \mathbf{T} + \mathbf{V}^X, X = \{A, B\}$. It should be noted that we have introduced the (AB) label, indicating that all the energies are computed by using fragment densities relaxed in the dimer electronic structure.

The partitioning in Eq. (7a) provides the basis for an energy-based localization of the MOs on the specific fragment regions (A and B). In fact, a rotation among the occupied MOs does not change the total energy. Thus, by minimizing the sum of the fragment energies ($E^A + E^B$) in the space spanned by the occupied MOs, their interaction energy (E^{AB}_{int}), and thus their repulsion, is maximized while keeping the total energy E constant.[26,27,102] Therefore, the resulting MOs are confined to the pre-defined A and B spatial regions and those are maximally localized within the fragment space because they are obtained by maximizing the interaction between the two fragments. For this reason, by recalling the nomenclature introduced in Ref. 27 at the Hartree–Fock level, we name them Kohn–Sham Fragment Localized Molecular Orbitals (KS-FLMOs). In physical terms, the minimization of the local electronic energies of the fragments is carried out at the cost of maximizing the repulsion between them. A similar idea has also been proposed in Ref. 103 to separate the frozen density into isolated fragment contributions. We recall that by a rotation in the occupied MO space, the total density matrix $\mathbf{D} = \mathbf{D}_A + \mathbf{D}_B$ remains constant. Thus, the sum of the fragment energies [$E^A + E^B$ defined in Eqs. (7b) and (7c)] can be reformulated in terms of the total and A fragment density matrices

and functions by using Eq. (4) [$\mathbf{D}^B = \mathbf{D} - \mathbf{D}^A, \rho^B(\mathbf{r}) = \rho(\mathbf{r}) - \rho^A(\mathbf{r})$], yielding

$$\begin{aligned} E^A + E^B = {} & \mathrm{Tr}\,(\mathbf{V}^A - \mathbf{V}^B)\mathbf{D}^A + \mathrm{Tr}\,\mathbf{D}^A\mathbf{J}(\mathbf{D}^A) - c_x\,\mathrm{Tr}\,\mathbf{D}^A\mathbf{K}(\mathbf{D}^A) \\ & + \int \rho^A(\mathbf{r})\varepsilon_{xc}(\rho^A(\mathbf{r}))\mathrm{d}\mathbf{r} - \beta\,\mathrm{Tr}\,\mathbf{D}^A\mathbf{K}^{\mathrm{LR}}(\mathbf{D}^A) \\ & + \int (\rho(\mathbf{r}) - \rho^A(\mathbf{r}))\varepsilon_{xc}(\rho(\mathbf{r}) - \rho^A(\mathbf{r}))\mathrm{d}\mathbf{r} \\ & - \mathrm{Tr}\,\mathbf{D}^A\mathbf{J}(\mathbf{D}) + c_x\,\mathrm{Tr}\,\mathbf{D}^A\mathbf{K}(\mathbf{D}) + \beta\,\mathrm{Tr}\,\mathbf{D}^A\mathbf{K}^{\mathrm{LR}}(\mathbf{D}) \\ & + \mathrm{Tr}\,\mathbf{h}^B\mathbf{D} + \frac{1}{2}\,\mathrm{Tr}\,\mathbf{D}\mathbf{J}(\mathbf{D}) - \frac{1}{2}c_x\,\mathrm{Tr}\,\mathbf{D}\mathbf{K}(\mathbf{D}) \\ & - \frac{\beta}{2}\,\mathrm{Tr}\,\mathbf{D}\mathbf{K}^{\mathrm{LR}}(\mathbf{D}) + h^A_{nuc} + h^B_{nuc}. \end{aligned} \tag{8}$$

Since the total density matrix, and consequently, the total density function $\rho(\mathbf{r})$, remains constant, we can calculate the Fock matrix elements in atomic orbital basis (AO, $\{\chi_\mu\}$) by functionally differentiating the energy in Eq. (8) with respect to $\mathbf{D}^A$ and $\rho^A(\mathbf{r})$,

$$\begin{aligned} F_{\mu\nu} = {} & V^A_{\mu\nu} - V^B_{\mu\nu} + 2J_{\mu\nu}(\mathbf{D}^A) - 2c_xK_{\mu\nu}(\mathbf{D}^A) \\ & + \int v_{xc}(\rho^A(\mathbf{r}))\chi_\mu(\mathbf{r})\chi_\nu(\mathbf{r})\mathrm{d}\mathbf{r} - 2\beta K^{\mathrm{LR}}_{\mu\nu}(\mathbf{D}^A) \\ & - \int v_{xc}(\rho(\mathbf{r}) - \rho^A(\mathbf{r}))\chi_\mu(\mathbf{r})\chi_\nu(\mathbf{r})\mathrm{d}\mathbf{r} \\ & - J_{\mu\nu}(\mathbf{D}) + c_xK_{\mu\nu}(\mathbf{D}) + \beta K^{\mathrm{LR}}_{\mu\nu}(\mathbf{D}), \end{aligned} \tag{9}$$

where $v_{xc} = v_c + (1 - c_x)v_x$ is the exchange-correlation potential density. It should be noted that the last two terms are one-electron terms entering the Fock matrix since the total density matrix ($\mathbf{D}$) remains fixed during the SCF localization optimization.

In this work, the formulation of KS-FLMOs is presented for the particular case of two interacting fragments, which is used in the following for the numerical applications. However, the method is general and can be formulated to the general case of N interacting fragments, even covalently, similar to what we have previously reported in the HF framework.[27]

Summarizing, the KS-FLMOs are obtained by using the following computational protocol.

1. Partitioning of a given idempotent AO density matrix of a dimer into A and B density matrices, using Cholesky decomposition for the A and B occupied orbitals.[14,99,104–107] To obtain the guess orthogonal orbitals, other methods can also be exploited, for instance, by resorting to MO localization procedures.[26] However, the Cholesky decomposition is unique if the same pivots are used and guarantees the potential energy surface continuity as compared to other localization procedures.[26] Generally, the density matrix of the dimer is obtained by minimizing the total DFT energy defined in Eq. (1). However, different density matrices can be exploited, as it is done in multilevel methods.[100,101] The Cholesky decomposition is performed by selecting the diagonal elements corresponding to the AO basis functions centered on the pre-defined A and B atoms.[96,99,100] In particular, $\mathbf{D}^A$ is calculated in the AO basis $\{\mu, \nu\}$ by a partial Cholesky decomposition of the total density matrix $\mathbf{D}$ as[97]

$$\sum_{IJ} D_{\mu I}\tilde{D}^{-1}_{IJ}D_{\nu J} = \sum_I L_{\mu I}L_{\nu I} = D^A_{\mu\nu}, \tag{10}$$

where I and J are the diagonal elements (selected among the AOs centered on the pre-defined A and B atoms), which are Cholesky decomposed, $\tilde{\mathbf{D}}$ is the submatrix of $\mathbf{D}$ containing the selected diagonal elements, and $L_{\alpha I}$ are the resulting Cholesky orbitals of the A fragment. The number of $\mathbf{D}$ diagonal elements that are selected corresponds to the number of occupied orbitals of the A fragment (n^A_o). This means that the largest n^A_o diagonal elements are selected. The B density matrix $\mathbf{D}^B = \mathbf{D} - \mathbf{D}^A$ is then Cholesky decomposed by considering the n^B_o largest diagonal elements belonging to B atoms.[26] As a result of the decomposition, the A and B Cholesky MOs are obtained, and the A and B density matrices $\mathbf{D}^A$, $\mathbf{D}^B$ are constructed [see Eq. (10)]. It should be noted that both fragment MOs and density matrices are defined in the full AO basis set.
2. From the two Cholesky decompositions, A and B occupied MOs are obtained, and the space spanned by the occupied MOs is thus defined. The local energy of the two fragments is minimized [see Eqs. (8) and (9)] in the MO space defined. The equations are solved in the reduced occupied space by transforming the AO basis through the A and B MO coefficients. The KS-FLMOs are the MOs obtained at convergence. The whole computational cost of the localization procedure is generally lower than that associated with a DFT energy minimization on the whole system.

B. Energy decomposition analysis based on KS-FLMOs

The KS-FLMOs provide a valuable basis for decomposing the interaction energy of two fragments into diverse energetic components. We name the resulting EDA Kohn–Sham fragment EDA (KS-FEDA) to highlight its grounds on KS-FLMOs. The interaction energy can be written as

$$\begin{aligned} E^{int} &= E - E^A_{(0)} - E^B_{(0)} \\ &= E^{AB}_{int,(AB)} + E^A_{(AB)} - E^A_{(0)} + E^B_{(AB)} - E^B_{(0)}, \end{aligned} \tag{11}$$

where E is the full DFT-optimized energy, whereas $E^A_{(0)}$ and $E^B_{(0)}$ are the energy of isolated A and B fragments in the gas phase. In this work, the basis set superposition error (BSSE) is reduced by means of the counterpoise correction proposed by Boys and Bernardi,[108] i.e., $E^A_{(0)}$ and $E^B_{(0)}$ are computed in the full AO basis set. By using the definition of $E^{AB}_{int,(AB)}$ [see Eq. (7d), readjusted in a GKS framework] and $E^{AB}_{\mathrm{non-add}}$ [see Eq. (6)], Eq. (11) can be rewritten as

$$E^{int} = E^{ele}_{(AB)} + E^{HF,x}_{(AB)} + E^{corr}_{(AB)} + E^{el-prep}_{(AB)}, \tag{12a}$$

$$E^{ele}_{(AB)} = \mathrm{Tr}\,\mathbf{D}^A_{(AB)}\mathbf{J}(\mathbf{D}^B_{(AB)}) + \mathrm{Tr}\,\mathbf{V}^A\mathbf{D}^B_{(AB)} + \mathrm{Tr}\,\mathbf{V}^B\mathbf{D}^A_{(AB)} + h^{AB}_{\mathrm{rep}}, \tag{12b}$$

$$E^{HF,x}_{(AB)} = -\mathrm{Tr}\,\mathbf{D}^A_{(AB)}\mathbf{K}(\mathbf{D}^B_{(AB)}), \tag{12c}$$

$$E^{corr}_{(AB)} = E^{xc}_{(AB)} - (1 - c_x)E^{HF,x}_{(AB)}, \tag{12d}$$

$$E^{el-prep}_{(AB)} = E^A_{(AB)} - E^A_{(0)} + E^B_{(AB)} - E^B_{(0)}, \tag{12e}$$

where

$$E^{xc}_{(AB)} = \int \rho(\mathbf{r})\varepsilon_{xc}(\rho(\mathbf{r}))\mathrm{d}\mathbf{r} - \int \rho^{A}_{(AB)}(\mathbf{r})\varepsilon_{xc}(\rho^{A}_{(AB)}(\mathbf{r}))\mathrm{d}\mathbf{r} - \int \rho^{B}_{(AB)}(\mathbf{r})\varepsilon_{xc}(\rho^{B}_{(AB)}(\mathbf{r}))\mathrm{d}\mathbf{r} - \beta\,\mathrm{Tr}\;\mathbf{D}^{A}\mathbf{K}^{\mathrm{LR}}(\mathbf{D}^{B}) = E_{xc}[\mathbf{D}] - E_{xc}[\mathbf{D}^{A}] - E_{xc}[\mathbf{D}^{B}]. \quad (13)$$

In Eq. (12a), the electrostatic $E^{ele}_{(AB)}$, the HF exchange $E^{HF,x}_{(AB)}$, the correlation $E^{corr}_{(AB)}$, and electronic preparation $E^{AB}_{el-prep}$ energies are introduced. It should be noted that we have used the same notation introduced in Eq. (7a); the subscript (AB) indicates that the electrostatic energy, exchange, and correlation terms are calculated by using the fragment densities as in the relaxed dimer electronic structure. The electrostatic energy comprises four terms: the electronic and nuclear repulsion energies and the nuclear–electron attraction contributions. The exchange–correlation energy term is decomposed according to a GKS framework [see also Eq. (1b)] in terms of a purely HF exchange and the correlation contribution of the specific DFT functional, similar to what has been proposed in Ref. 69. The electronic preparation energy represents the energy needed to deform the electron density of the two fragments from the vacuo to the supramolecular structure (AB) and is repulsive (positive) by construction. It is worth remarking that the decomposition presented in Eq. (12) represents the DFT extension of the LED approach presented in Ref. 64 defined at the HF/DPLNO-CCSD(T) level. For this reason, the energy partitioning in Eq. (12) is labeled KS-FEDA(LED).

Since the energetic contributions in Eq. (12a) are calculated using the relaxed fragment densities, they are not directly related to the energetic contributions that are commonly exploited in other EDA techniques, such as KM-EDA[47] and SAPT.[57,58] As an example, in most EDA schemes, the electrostatic energy is classically computed by considering the unperturbed isolated fragment densities (classical limit).[38] For this reason, in the following, we provide an additional partitioning of the KS-FEDA(LED) energy terms that physically describe how the intermolecular interaction terms change as the frozen fragment densities evolve into those within the dimer. The resulting energy decomposition terms, which properly define the KS-FEDA technique, will be directly compared to established EDA methods.

The fragment densities ($\mathbf{D}^{A}_{0}, \rho^{A}_{0}$ and $\mathbf{D}^{B}_{0}, \rho^{B}_{0}$) obtained by minimizing the energy of the two isolated fragments can be exploited to compute the frozen interaction energy components,

$$E^{int}_{(0)} = E^{ele}_{(0)} + E^{HF,x}_{(0)} + E^{corr}_{(0)}, \quad (14a)$$

$$E^{ele}_{(0)} = \mathrm{Tr}\;\mathbf{D}^{A}_{0}\mathbf{J}(\mathbf{D}^{B}_{0}) + \mathrm{Tr}\;\mathbf{V}^{A}\mathbf{D}^{B}_{0} + \mathrm{Tr}\;\mathbf{V}^{B}\mathbf{D}^{A}_{0} + h^{AB}_{\mathrm{rep}}, \quad (14b)$$

$$E^{HF,x}_{(0)} = -\mathrm{Tr}\;\mathbf{D}^{A}_{0}\mathbf{K}(\mathbf{D}^{B}_{0}), \quad (14c)$$

$$E^{corr}_{(0)} = E_{xc}[\mathbf{D}_0] - E_{xc}[\mathbf{D}^{A}_{0}] - E_{xc}[\mathbf{D}^{B}_{0}] - (1-c_x)E^{HF,x}_{(0)}, \quad (14d)$$

where the electronic preparation energy is zero by definition and $\mathbf{D}_0 = \mathbf{D}^{A}_{0} + \mathbf{D}^{B}_{0}$. As also pointed out by Head-Gordon and co-workers,[38,109] these quantities are properly defined only if the two fragment densities do not overlap. To get a more physically consistent picture, the antisymmetry of the total wave function needs to be taken into account. This can be imposed by first minimizing the energy of the two isolated fragments and then ortho-normalizing the MOs of the dimer (i.e., $\boldsymbol{\phi}_0 = \boldsymbol{\phi}^{A}_{0} \oplus \boldsymbol{\phi}^{B}_{0}$) by means of a Löwdin procedure[110] ($\bar{\boldsymbol{\phi}}_{\mathrm{ASN}} = \mathbf{S}^{\frac{1}{2}}\boldsymbol{\phi}^{AB}_{0}$, where $\mathbf{S}$ is the overlap matrix). The density matrix and the density function associated with the antisymmetrized (ASN) wavefunction can then be calculated as

$$\mathbf{D}_{\mathrm{ASN}} = 2\mathbf{C}\mathbf{S}^{-1}\mathbf{C}, \quad (15a)$$

$$\rho_{\mathrm{ASN}}(\mathbf{r}) = \sum_{\mu,\nu} D_{\mathrm{ASN},\mu\nu}\chi_{\mu}(\mathbf{r})\chi_{\nu}(\mathbf{r}), \quad (15b)$$

where $\mathbf{C}$ are the MO coefficients of the isolated monomers. It should be noted that $\mathbf{D}_{\mathrm{ASN}}$ represents the physically valid single determinant density matrix belonging to the frozen fragment orbitals. The related energy E^{ASN} is computed by substituting $\mathbf{D}^{\mathrm{ASN}}$ and ρ^{ASN} in Eq. (1). As a result of applying the antisymmetry operator, a delocalized wavefunction is obtained. A KS-FLMO localization procedure is thus performed to obtain the density matrices ($\mathbf{D}^{A}_{\mathrm{ASN}}, \mathbf{D}^{B}_{\mathrm{ASN}}$) and energies ($E^{A}_{\mathrm{ASN}}, E^{B}_{\mathrm{ASN}}$) of the fragments in the electronic structure of the antisymmetrized dimer. In this way, the ASN energy E^{ASN} can be decomposed into the electrostatic, HF exchange, correlation, and electronic preparation energies as

$$E^{int}_{\mathrm{ASN}} = E^{ele}_{\mathrm{ASN}} + E^{HF,x}_{\mathrm{ASN}} + E^{corr}_{\mathrm{ASN}} + E^{el-prep}_{\mathrm{ASN}}, \quad (16a)$$

$$E^{ele}_{\mathrm{ASN}} = \mathrm{Tr}\;\mathbf{D}^{A}_{\mathrm{ASN}}\mathbf{J}(\mathbf{D}^{B}_{\mathrm{ASN}}) + \mathrm{Tr}\;\mathbf{V}^{A}\mathbf{D}^{B}_{\mathrm{ASN}} + \mathrm{Tr}\;\mathbf{V}^{B}\mathbf{D}^{A}_{\mathrm{ASN}} + h^{AB}_{\mathrm{rep}}, \quad (16b)$$

$$E^{HF,x}_{\mathrm{ASN}} = -\mathrm{Tr}\;\mathbf{D}^{A}_{\mathrm{ASN}}\mathbf{K}(\mathbf{D}^{B}_{\mathrm{ASN}}), \quad (16c)$$

$$E^{corr}_{\mathrm{ASN}} = E_{xc}[\mathbf{D}_{\mathrm{ASN}}] - E_{xc}[\mathbf{D}^{A}_{\mathrm{ASN}}] - E_{xc}[\mathbf{D}^{B}_{\mathrm{ASN}}] - (1-c_x)E^{HF,x}_{\mathrm{ASN}}, \quad (16d)$$

$$E^{el-prep}_{\mathrm{ASN}} = E^{A}_{\mathrm{ASN}} - E^{A}_{(0)} + E^{B}_{\mathrm{ASN}} - E^{B}_{(0)}. \quad (16e)$$

By combining Eqs. (14) and (16), E^{int}_{ASN} can be rewritten as

$$E^{int}_{\mathrm{ASN}} = E^{ele}_{(0)} + E^{HF,x}_{(0)} + E^{corr}_{(0)} + \Delta E_{\mathrm{ASN}}. \quad (17)$$

Here, ΔE_{ASN} represents the energy variation due to the antisymmetrization of the dimer wavefunction. It can be decoupled into electrostatic, HF exchange, and correlation contributions,

$$\Delta E_{\mathrm{ASN}} = \Delta E^{ele}_{\mathrm{ASN}} + \Delta E^{HF,x}_{\mathrm{ASN}} + E^{el-prep}_{\mathrm{ASN}} + \Delta E^{corr}_{\mathrm{ASN}} = \Delta E^{HF}_{\mathrm{ASN}} + \Delta E^{corr}_{\mathrm{ASN}}, \quad (18a)$$

$$\Delta E^{ele}_{\mathrm{ASN}} = E^{ele}_{\mathrm{ASN}} - E^{ele}_{(0)}, \quad (18b)$$

$$\Delta E^{HF,x}_{\mathrm{ASN}} = E^{HF,x}_{\mathrm{ASN}} - E^{HF,x}_{(0)}, \quad (18c)$$

$$\Delta E^{corr}_{\mathrm{ASN}} = E^{corr}_{\mathrm{ASN}} - E^{corr}_{(0)}. \quad (18d)$$

Using Eq. (18), we can introduce in Eq. (17) the electrostatic ($E^{ele} = E^{ele}_{(0)}$), exchange ($E^{ex} = E^{HF,x}_{(0)}$), and repulsion ($E^{rep} = \Delta E^{HF}_{\rm ASN}$) quantities that are commonly exploited in other EDA techniques,

$$E^{int}_{\rm ASN} = E^{ele} + E^{ex} + E^{rep} + E^{corr}_{\rm ASN}. \tag{19}$$

Equation (19) highlights that the repulsion energy is associated with the energy increase resulting from the antisymmetrization of the total wavefunction, i.e., by the inclusion of Pauli repulsion.

By combining Eqs. (12) and (19), we can decompose the total interaction energy [see Eq. (11)] as follows:

$$E^{int} = E^{ele} + E^{ex} + E^{rep} + E^{corr}_{ASN} + \Delta E_{\rm orb}, \tag{20}$$

where $\Delta E_{\rm orb}$ accounts for the interaction energy due to the orbital relaxation and reads

$$\begin{aligned}\Delta E_{\rm orb} &= \Delta E^{ele}_{\rm orb} + \Delta E^{HF,x}_{\rm orb} + \Delta E^{el-prep}_{\rm orb} + \Delta E^{corr}_{\rm orb} \\ &= \Delta E^{HF}_{\rm orb} + \Delta E^{corr}_{\rm orb},\end{aligned} \tag{21a}$$

$$\Delta E^{ele}_{\rm orb} = E^{ele}_{(AB)} - E^{ele}_{\rm ASN}, \tag{21b}$$

$$\Delta E^{HF,x}_{\rm orb} = E^{HF,x}_{(AB)} - E^{HF,x}_{\rm ASN}, \tag{21c}$$

$$\Delta E^{el-prep}_{\rm orb} = E^{el-prep}_{(AB)} - E^{el-prep}_{\rm ASN}, \tag{21d}$$

$$\Delta E^{corr}_{\rm orb} = E^{corr}_{(AB)} - E^{corr}_{\rm ASN}. \tag{21e}$$

As for the other energy components, the total orbital relaxation energy can be decomposed in the variations of electrostatic ($\Delta E^{ele}_{\rm orb}$), HF exchange ($\Delta E^{HF,x}_{\rm orb}$), correlation energy ($\Delta E^{corr}_{\rm orb}$), and electronic preparation energy ($\Delta E^{el-prep}_{\rm orb}$). These components capture the energetics associated with the relaxation of the electronic structure as the orbitals relax to their new equilibrium minimum following the minimization of the dimer energy. In passing, we note that similar orbital relaxation energy terms have been introduced for the LED method at the HF level.[67] Equation (20) can thus be rewritten by inserting $E^{corr}_{(AB)} = E^{corr}$ [see Eq. (12d)], yielding a five-term EDA,

$$E^{int} = E^{ele} + E^{ex} + E^{rep} + E^{corr} + \Delta E^{HF}_{\rm orb}, \tag{22}$$

where E^{ex} and E^{rep} can also be combined together as it is done in most EDA schemes, such as KM-EDA and SAPT.

Our decomposition also allows for an equivalent 11-term EDA decomposition that can be obtained by combining Eq. (22) with Eqs. (18) and (21),

$$\begin{aligned}E^{int} = {} & E^{ele} + E^{ex} + E^{corr}_{(0)} + \Delta E^{ele}_{\rm ASN} + \Delta E^{HF,x}_{\rm ASN} + E^{el-prep}_{\rm ASN} + \Delta E^{corr}_{\rm ASN} \\ & + \Delta E^{ele}_{\rm orb} + \Delta E^{HF,x}_{\rm orb} + \Delta E^{el-prep}_{\rm orb} + \Delta E^{corr}_{\rm orb}.\end{aligned} \tag{23}$$

Such an expansion is particularly useful because it allows for an in-depth investigation of the physicochemical origin of the $E^{rep} = \Delta E^{HF}_{\rm ASN}$ and $\Delta E^{HF}_{\rm orb}$ energy terms, which differentiates the proposed EDA technique from most other EDA methods. Equations (22) and (23) represent the final KS-FEDA partitioning, which physically takes into account how the interaction energy terms change as the densities of the monomers evolve as the adduct is electronically formed. In such a picture, the energy contributions defined at the KS-FEDA(LED) level [Eq. (12)] represent the interaction terms for monomers' densities in the final electronic structure of the dimer. In other words, by exploiting Eq. (23) (which defines all the terms defined in KS-FEDA) KS-FEDA(LED) energy terms have been decomposed into their frozen, ASN, and orbital-relaxation contributions as

$$E^{ele}_{(AB)} = E^{ele} + \Delta E^{ele}_{\rm ASN} + \Delta E^{ele}_{\rm orb}, \tag{24a}$$

$$E^{HF,x}_{(AB)} = E^{ex} + \Delta E^{HF,x}_{\rm ASN} + \Delta E^{HF,x}_{\rm orb}, \tag{24b}$$

$$E^{corr}_{(AB)} = E^{corr}_{(0)} + \Delta E^{corr}_{\rm ASN} + \Delta E^{corr}_{\rm orb}, \tag{24c}$$

$$E^{el-prep}_{(AB)} = E^{el-prep}_{\rm ASN} + \Delta E^{el-prep}_{\rm orb}. \tag{24d}$$

Finally, it is known that most DFT functionals cannot properly describe dispersion interactions. In this work, the dispersion interaction is treated by using the empirical D4 method, an effective parameter-dependent approach that does not depend on molecular densities. The interaction dispersion energy E^{disp} reads

$$E^{disp} = E^{disp}_{AB} - E^{disp}_{A} - E^{disp}_{B}, \tag{25}$$

where E^{disp}_{A} and E^{disp}_{B} are the dispersion energies of the A and B monomers, respectively, while E^{disp}_{AB} is that of the dimer. It should be noted that the dispersion contribution can also be introduced by exploiting more sophisticated, yet additive, approaches, such as the mothod by Tkatchenko–Scheffler[74] or many-body dispersion.[75] In addition, dispersion-corrected density functionals can be used,[76] which will include the dispersion energy contribution in the correlation term.

By inserting E^{disp} in Eqs. (12), (22), and (23), the KS-FEDA(LED) and the 6- and 12-term KS-FEDA are obtained

$$E^{int} = E^{ele}_{(AB)} + E^{HF,x}_{(AB)} + E^{corr}_{(AB)} + E^{el-prep}_{(AB)} + E^{disp}, \tag{26a}$$

$$E^{int} = E^{ele} + E^{ex} + E^{rep} + E^{corr} + \Delta E^{HF}_{\rm orb} + E^{disp}, \tag{26b}$$

$$\begin{aligned}E^{int} = {} & E^{ele} + E^{ex} + E^{corr}_{(0)} \\ & + \Delta E^{ele}_{\rm ASN} + \Delta E^{HF,x}_{\rm ASN} + E^{el-prep}_{\rm ASN} + \Delta E^{corr}_{\rm ASN} \\ & + \Delta E^{ele}_{\rm orb} + \Delta E^{HF,x}_{\rm orb} + \Delta E^{el-prep}_{\rm orb} + \Delta E^{corr}_{\rm orb} + E^{disp}.\end{aligned} \tag{26c}$$

The energetic components defined in Eq. (26b) can be directly compared to most EDA techniques and closely recall GKS-EDA,[69] with a different procedure to calculate repulsion and orbital-relaxation energy terms.

We remark that the energetic components in Eq. (26) are defined for a generic hybrid DFT functional. However, the method

is general and can thus be also applied to an HF wavefunction by imposing $\varepsilon_{xc} = 0$; $c_x = 1$. In this case, all E^{corr} contributions vanish.

In summary, the density evolution from frozen isolated fragments to the final electronic structure of the dimer is computed by performing the following steps, which provide all KS-FEDA energy terms:

1. Minimization of isolated A and B DFT energies (E_0^A and E_0^B) in the full AO basis set to minimize the BSSE.
2. Calculation of the interaction frozen energy terms through Eq. (14) by using the obtained A and B density matrices $\mathbf{D}_0^A$ and $\mathbf{D}_0^B$.
3. Antisymmetrization of the total wavefunction using the Löwdin procedure and construction of the ASN density matrix [$\mathbf{D}_{\mathrm{ASN}}$ – Eq. (15a)].
4. KS-FLMO localization using the ASN density matrix (see Sec. II A) to obtain the fragment density matrices ($\mathbf{D}^A_{\mathrm{ASN}}, \mathbf{D}^B_{\mathrm{ASN}}$) and energies ($E^A_{\mathrm{ASN}}, E^B_{\mathrm{ASN}}$) in the electronic structure of the ASN dimer.
5. Calculation of the interaction energy terms related to the antisymmetrization of the dimer wavefunction by exploiting Eqs. (16) and (18).
6. Minimization of the total system DFT energy E [see Eq. (1)].
7. KS-FLMO localization of the total system density matrix $\mathbf{D}$ (see Sec. II A) to obtain the fragment density matrices ($\mathbf{D}^A_{(AB)}, \mathbf{D}^B_{(AB)}$) and energies ($E^A_{(AB)}, E^B_{(AB)}$) in the relaxed electronic structure of dimer.
8. Calculation of KS-FEDA(LED) interaction energy terms in Eq. (12) and those related to the orbital relaxation by using Eq. (21).

It is worth remarking that for computing KS-FEDA(LED) terms in Eq. (26a), steps 1, 6, 7, and 8 are only required.

C. Solvent effects in KS-FEDA

Similar to most electronic properties, interaction energies are affected by the surrounding environment.[36,70,111–113] In this work, such effects are included by means of the polarizable continuum model (PCM),[83–85] which models the environment as a continuum dielectric characterized by a static dielectric constant (ε) and is generally applied to solutions. The total system is thus divided into a QM part (the solute), which is accommodated into a molecular-shaped cavity, interacting with the external solvent treated as a continuum. A surface density on the cavity arises as a response to the electrostatic potential generated by the QM density. Such density then perturbs the QM density in a mutual polarization fashion. Numerically, the cavity surface meshes into surface elements, called tesserae, and the surface density is discretized in a set of charges placed at the centers of each tesserae.

The interaction between the DFT and PCM parts is expressed in terms of the electrostatic interaction between the QM potential [$V_i(\mathbf{D})$ calculated by the QM density at the position of the ith charge] and the PCM charges $\boldsymbol{\sigma}$,[83]

$$E_{DFT/PCM}[\mathbf{D}] = \sum_i^{N_\sigma} \sigma_i(\mathbf{D}) V_i(\mathbf{D}). \tag{27}$$

In Eq. (27), we have made explicit that the PCM charges depend on the QM density $\mathbf{D}$. In fact, the PCM charges are obtained by solving the following set of linear equations (in a vector notation):[83]

$$\mathbf{T}\boldsymbol{\sigma} = -\mathbf{R}\mathbf{V}(\mathbf{D}), \tag{28}$$

where the matrices $\mathbf{T}$ and $\mathbf{R}$ depend on the cavity geometrical factors and the dielectric constant ε of the considered solvent.[83] The solvation energy is calculated as half the electrostatic interaction energy between the QM density and the PCM charges as[83]

$$E^{PCM}[\mathbf{D}] = \frac{1}{2}\boldsymbol{\sigma}(\mathbf{D})\mathbf{V}(\mathbf{D}). \tag{29}$$

The KS-FLMO localization procedure for a DFT/PCM calculation does not require any modification because the PCM term defined in Eq. (27) depends on the total density matrix $\mathbf{D}$. Thus, such a term remains constant during the localization procedure to obtain the KS-FLMOs. Therefore, Eqs. (8) and (9) are not directly affected by the presence of the environment, which only modifies the MOs and the associated densities.

Differently, the interaction energy E^{int} between two QM fragments varies due to the presence of the surrounding PCM layer via an explicit solvation energy term [Eq. (29)]. The proposed KS-FEDA is thus modified by inserting three additional terms related to the solvation contributions,

$$E^{int} = E^{ele} + E^{ex} + E^{rep} + E^{corr} + \Delta E^{HF}_{\mathrm{orb}} + E^{solv} + E^{disp}, \tag{30a}$$

$$\begin{aligned} E^{int} = {} & E^{ele} + E^{ex} + E^{solv}_{(0)} + E^{corr}_{(0)} \\ & + \Delta E^{ele}_{\mathrm{ASN}} + \Delta E^{HF,x}_{\mathrm{ASN}} + E^{el-prep}_{\mathrm{ASN}} + \Delta E^{corr}_{\mathrm{ASN}} + \Delta E^{solv}_{\mathrm{ASN}} \\ & + \Delta E^{ele}_{\mathrm{orb}} + \Delta E^{HF,x}_{\mathrm{orb}} + \Delta E^{el-prep}_{\mathrm{orb}} + \Delta E^{corr}_{\mathrm{orb}} + \Delta E^{solv}_{\mathrm{orb}} + E^{disp}, \end{aligned} \tag{30b}$$

where E^{solv}, $E^{solv}_{(0)}$, $\Delta E^{solv}_{\mathrm{ASN}}$, and $\Delta E^{solv}_{\mathrm{orb}}$ read [using Eq. (29)]

$$E^{solv} = E^{solv}_{(0)} + \Delta E^{solv}_{\mathrm{ASN}} + \Delta E^{solv}_{\mathrm{orb}}, \tag{31a}$$

$$E^{solv}_{(0)} = E^{PCM}[\mathbf{D}^A_0 + \mathbf{D}^B_0] - E^{PCM}[\mathbf{D}^A_0] - E^{PCM}[\mathbf{D}^B_0], \tag{31b}$$

$$\Delta E^{solv}_{\mathrm{ASN}} = E^{PCM}[\mathbf{D}_{\mathrm{ASN}}] - E^{PCM}[\mathbf{D}^A_0 + \mathbf{D}^B_0], \tag{31c}$$

$$\Delta E^{solv}_{\mathrm{orb}} = E^{PCM}[\mathbf{D}] - E^{PCM}[\mathbf{D}_{\mathrm{ASN}}]. \tag{31d}$$

To account for the solvent effects, the computational protocol sketched in Sec. II B is thus modified by including the defined frozen, ASN, and orbital relaxation energy terms associated with solvent effects in steps 2, 5, and 8. As specified in Sec. II B, the DFT energy of the isolated fragments is minimized in the full AO basis set to reduce the BSSE. In a DFT/PCM calculation for a dimer system in the equilibrium geometry, this means that the PCM cavity used in the monomers calculation is the same as in the dimer case. As a consequence, similarly to Ref. 113, cavitation effects associated with the formation of the dimer cavity are not taken into account in our approach.

We finally remark that in addition to the direct solvation contributions to the interaction energy defined in Eq. (31), the inclusion of solvent effects also perturbs the fragment densities, MOs and FLMOs, thus indirectly affecting all energetic terms in Eq. (30). It is worth noting that this is close to what has been proposed in the

context of ALMO-EDA,[112] which provides a similar ASN solvation energy ($E^{solv}_{ASN} = E^{solv}_{(0)} + \Delta E^{solv}_{ASN}$), which also accounts for cavitation effects related to the formation of the dimer cavity.

III. COMPUTATIONAL DETAILS

The procedure to obtain KS-FLMOs and the associated KS-FEDA is implemented in a development version of the electronic structure code $e^{\mathcal{T}}$.[114] To showcase the method, we select two datasets widely exploited to study non-covalent interactions in molecular systems. In particular, we use the A24 and S22 datasets, two sets of bimolecular systems consisting of 24 (A24)[87] and 22 (S22)[88] dimers. The A24 dataset is a set of non-covalent complexes specifically designed to benchmark computational methods against highly accurate calculations.[87] It encompasses various types of non-covalent interactions, making it suitable for testing the accuracy of novel theoretical approaches such as KS-FEDA. In particular, in Ref. 87, the 24 dimers are partitioned into three families: five hydrogen-bonded (HB), ten mixed electrostatics/dispersion interactions (MX), and nine dispersion-dominated (DD, including $\pi - \pi$ stacking). In Fig. 1, we show a graphical depiction of the A24 dataset, with a color map depending on the classification of Ref. 87 (blue, HB; green, MX; and salmon, DD). All the A24 geometries are recovered from Ref. 87.

The S22 dataset[88] comprises 22 complexes characterized by HB, DD, and MX non-covalent interactions. This dataset has been amply exploited in testing and benchmarking the accuracy of various computational methods for non-covalent interactions.[63,115,116] The S22 dataset is composed of systems of larger size than A24, up to 30 atoms (thymine-adenine S15). Similar to A24, we provide a graphical depiction of S22 dimers shown in Fig. 2, where the same color code introduced above is used according to the classification proposed in Ref. 88. All the S22 geometries are recovered from Ref. 88.

To further investigate the performance of KS-FEDA, we also consider the IHB15 dataset,[89] which is composed of 15 complexes characterized by ionic hydrogen bonding non-covalent interactions. Ionic HB systems are studied for the different nature of the non-covalent interactions[117] compared to neutral A24 and S22 datasets. The IHB15 dataset covers charged acetate, methylammonium, guanidinium, and imidazolium, interacting with water, methanol, methylamine, and formaldehyde. Such a dataset has been specifically constructed to represent charged molecular systems that can be found in biomolecules, such as proteins.[89] Similar to A24 and S22, we provide a graphical depiction of IHB15 dimers in Fig. 3, where we color the dimers according to their total charge following the classification in Ref. 89, from which IHB15 geometries are recovered.

For each system, the B3LYP[118,119] and PBE0[120] hybrid functionals combined with the aug-cc-pVDZ and aug-cc-pVTZ basis sets are exploited to highlight the dependence of the computed energy components on the choice of basis sets and DFT functionals (Secs. S3–S8 in the supplementary material). For all systems, dispersion energies are calculated at the D4 level.[71–73] For the sake

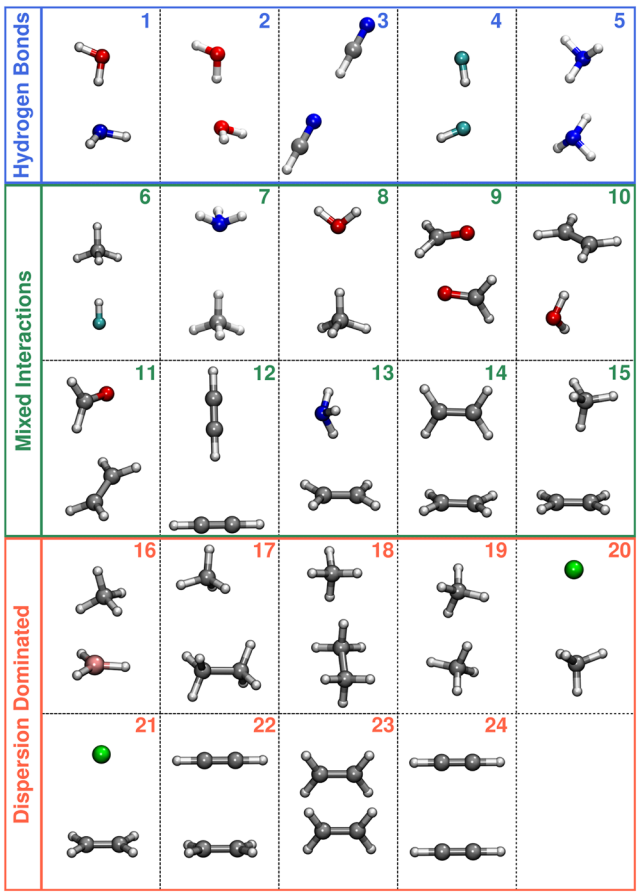

FIG. 1. Graphical representation of the A24 dataset. The dimers are grouped according to the classification provided in Ref. 87.

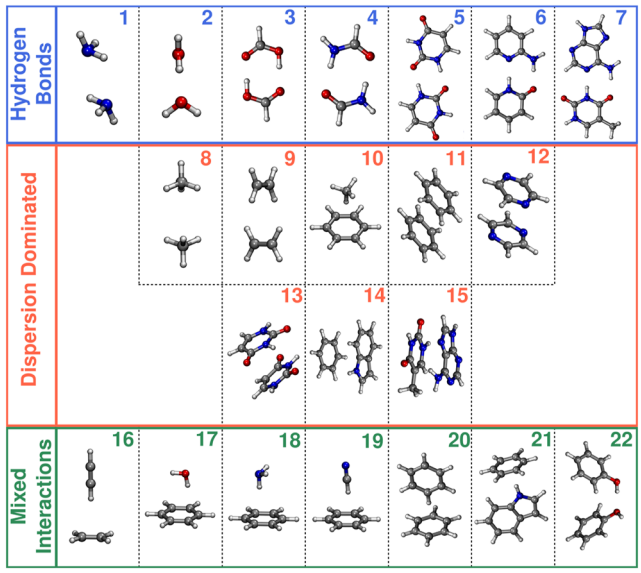

FIG. 2. Graphical representation of the S22 dataset. The dimers are grouped according to the classification provided in Ref. 88.

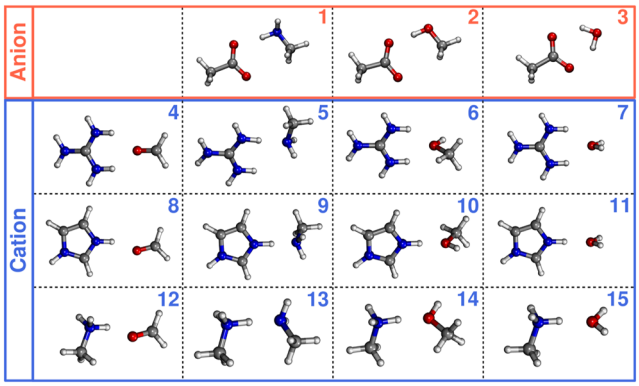

FIG. 3. Graphical representation of the IHB15 dataset. The dimers are grouped according to the classification provided in Ref. 89.

of comparison, the interaction energy is also decomposed at the SAPT(DFT) for the neutral couples (A24 and S22), using both B3LYP and PBE0 functionals, and SAPT2+(3)δMP2 levels (for all dimers) in combination with aug-cc-pVDZ and aug-cc-pVTZ basis sets. SAPT2+(3)δMP2/aug-cc-pVTZ is selected as it is considered the golden standard for SAPT methods.[63] All the SAPT calculations are performed by using Psi4 1.9.[121,122] For SAPT(DFT) calculations, we compute the ionization potential shift by subtracting the HOMO energies of each monomer and reference data recovered from the NIST database[123] (see Secs. S3–S6 in the supplementary material, where raw data are reported).

To showcase how solvent effects can affect intermolecular interactions and their components, we select water as solvent ($\varepsilon = 78.39$) described using IEFPCM[86] as implemented in PCMSolver,[124,125] which is interfaced to e$^{\mathscr{T}}$.[114] The PCM cavity is constructed by using UFF radii.[126] For each dimer, the dimer geometries are kept frozen to those of the gas phase; thus, solvent effects only affect the electronic structure of the dimers.

IV. NUMERICAL APPLICATIONS

In this section, we first analyze the dependence of KS-FEDA energy contributions on the basis set and the DFT functionals (GGA, hybrid, and range-separated). The distance dependence of the KS-FEDA energy terms is then analyzed for a water dimer (structure 2 of the A24 dataset). Finally, KS-FEDA is exploited to study the non-covalent interactions of the A24, S22, and IHB15 datasets, and the quality of the method is assessed by comparing it to established EDA approaches, such as SAPT(DFT) and SAPT2+(3)δMP2.

A. KS-FEDA dependence on basis set and DFT functional

We start our discussion by first analyzing the dependence of KS-FEDA energy terms on the basis set. KS-FEDA is based on counterpoise-corrected energies; thus, the BSSE is substantially reduced. However, the energy contributions might still be influenced by basis set incompleteness error (BSIE). To examine the BSIE impact on KS-FEDA energy contributions, we consider the water–ammonia and methane dimers (structures 1 and 19 of the A24 datasets), as previously done in Ref. 64 at the LED level. Such systems are chosen as representative of weak interactions, such as hydrogen bonding (water-ammonia) and dispersion (methane dimer). The KS-FEDA(LED) energy terms computed by using the B3LYP functional are provided in Table I as combined with cc-pVXD and aug-cc-pVXD basis sets (X = D, T, Z). All the KS-FEDA energy

TABLE I. Dependence of KS-FEDA(LED) energy terms on the basis set.

Basis-set	E^{int}	$E^{ele}_{(AB)}$	$E^{HF,x}_{(AB)}$	$E^{corr}_{(AB)}$	$E^{el-prep}_{(AB)}$
			CH_4–CH_4		
cc-pVDZ	0.45	−1.11	−0.62	−0.11	2.29
cc-pVTZ	0.46	−1.14	−0.69	−0.08	2.37
cc-pVQZ	0.47	−1.14	−0.69	−0.08	2.38
aug-cc-pVDZ	0.47	−1.11	−0.69	−0.06	2.33
aug-cc-pVTZ	0.46	−1.15	−0.69	−0.09	2.39
aug-cc-pVQZ	0.46	−1.15	−0.69	−0.09	2.39
			NH_3–H_2O		
cc-pVDZ	−5.81	−35.90	−7.74	−2.57	40.40
cc-pVTZ	−5.81	−35.68	−7.54	−2.52	39.92
cc-pVQZ	−5.92	−35.72	−7.52	−2.51	39.83
aug-cc-pVDZ	−5.96	−35.25	−7.60	−2.53	39.42
aug-cc-pVTZ	−6.05	−35.87	−7.54	−2.50	39.86
aug-cc-pVQZ	−6.06	−35.91	−7.53	−2.50	39.87

terms [see Eq. (26c)] are presented in Table S1 in the supplementary material.

Table I presents the KS-FEDA(LED) basis set convergence behavior for these systems. The interaction energy and its constituent components rapidly converge with increasing basis set size, especially when augmented basis sets are exploited. Furthermore, the qualitative trends remain consistent across all tested basis sets. For the weakly interacting methane dimer, the maximum change from the cc-pVDZ to cc-pVQZ basis set is 0.09 kcal/mol for $E^{el-prep}_{(AB)}$, which reduces to 0.06 kcal/mol when augmented basis are considered. For the strongly interacting water–ammonia system at the cc-pVXZ level, the convergence behavior is slightly less favorable for both ΔE_{int} and its components, although the results remain stable with the maximum variation (0.57 kcal/mol) reported for the $\Delta E^{el-prep}_{(AB)}$ term. Such findings are consistent with what has been reported at the LED level in Ref. 64. A much better convergence is achieved by using aug-cc-pVXZ basis sets, for which converged results of all energy components are displayed by using the aug-cc-pVTZ basis set [maximum discrepancy of 0.04 kcal/mol for $E^{ele}_{(AB)}$]. For this reason, in all the following calculations, we exploit the aug-cc-pVTZ basis-set, for which the BSIE is negligible.

We now move to study KS-FEDA(LED) energy terms dependence on the DFT functionals. To demonstrate the flexibility of the KS-FEDA scheme, we select GGA (B97[127]), hybrid (B3LYP, PBE0), and range-separated (CAM-B3LYP,[93] ωB97xD[92]) functionals. Dispersion interactions are considered by using D2 (ωB97xD[92]), D3 (B97), or D4 (B3LYP, PBE0, CAM-B3LYP) corrections. The KS-FEDA(LED) energy terms computed by using the aug-cc-pVTZ basis set are presented in Table I. All the KS-FEDA energy terms [see Eq. (26c)] are reported in Table S2 in the supplementary material.

As expected, Table II shows that the computed interaction energy for the two considered dimers depends on the chosen functional. For the weakly interacting methane dimer, B97 reports the largest absolute interaction energy; the opposite holds for the water–ammonia case. B3LYP predicts the most repulsive interaction energy for the methane dimer, while the most attractive energy for the HB system is reported by CAM-B3LYP. Although such differences are also reflected in the KS-FEDA(LED) energy contributions, the qualitative description provided by all functionals is very similar, especially when combining together the correlation and dispersion contributions ($E^{corr}_{(AB)} + E^{disp}$). In fact, while for $E^{ele}_{(AB)}$, $E^{HF,x}_{(AB)}$, and $E^{el-prep}_{(AB)}$, a qualitative agreement between all functionals is obtained, $E^{corr}_{(AB)}$ reflects the physical differences between the functionals in describing correlation effects. This is particularly evident by moving from B97 (GGA) to hybrid functionals for both systems. The underestimation of correlation effects is generally compensated by the empirical dispersion correction, which, as expected, is again dependent on the DFT functional exploited.

B. Distance dependence of KS-FEDA energy terms

In this section, we discuss the dependence of the KS-FEDA(LED) energy terms on the intermolecular distance (d). To this end, we consider a water dimer (structure 2 – A24 dataset) following the analysis reported in Ref. 128 at the LED level. The KS-FEDA is performed at the B3LYP-D4/aug-cc-pVTZ level, and the resulting KS-FEDA(LED) energy terms as a function of the O···H distance are shown in Fig. 4 (from 1.5 to 6 Å, step 0.05 Å, raw data provided in Table S3 in the supplementary material). In the left panel, $E^{ele}_{(AB)}$ and $E^{el-prep}_{(AB)}$ are reported, while the remaining $E^{corr}_{(AB)}$, $E^{HF,x}_{(AB)}$, and E^{disp} are given in the right panel.

In the long range ($d \geq 3.5$ Å), the only significant KS-FEDA(LED) term is the electrostatic energy. As expected due to the strong dipole moment of water, in this region, $E^{ele}_{(AB)}$ exhibits a slow polynomial decay with the distance. This can be further

TABLE II. Dependence of KS-FEDA(LED)/aug-cc-pVTZ energy terms on the DFT functional.

Functional	E^{int}	$E^{ele}_{(AB)}$	$E^{HF,x}_{(AB)}$	$E^{corr}_{(AB)}$	$E^{el-prep}_{(AB)}$	E^{disp}
			CH_4–CH_4			
B97-D3	−0.63	−1.16	−0.69	0.05	2.43	−1.26
B3LYP-D4	−0.41	−1.15	−0.69	−0.09	2.39	−0.87
PBE0-D4	−0.56	−1.07	−0.66	−0.57	2.30	−0.56
CAM-B3LYP-D4	−0.48	−1.12	−0.68	−0.49	2.37	−0.58
ωB97xD	−0.56	−1.02	−0.63	−0.30	2.23	−0.84
			NH_3–H_2O			
B97-D3	−6.41	−38.00	−8.14	−1.38	42.45	−1.35
B3LYP-D4	−6.80	−35.87	−7.53	−2.50	39.86	−0.76
PBE0-D4	−7.11	−34.86	−7.25	−2.88	38.32	−0.43
CAM-B3LYP-D4	−7.14	−34.79	−7.16	−3.34	38.59	−0.43
ωB97xD	−6.76	−34.46	−7.09	−2.06	37.46	−0.61

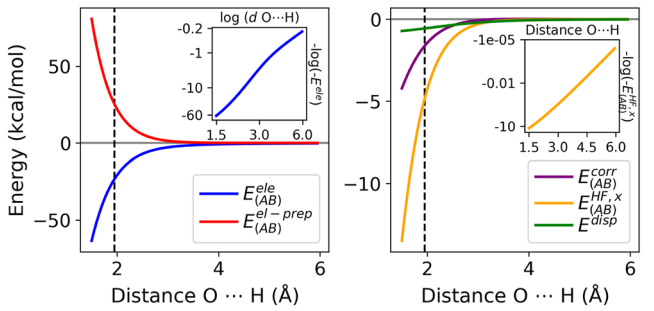

FIG. 4. KS-FEDA(LED) energy terms of water dimer as a function of the intermolecular distance. The log–log ($E^{ele}_{(AB)}$) and semi-log ($E^{HF,x}_{(AB)}$) plots are given as insets. The equilibrium distance is indicated by the dotted vertical line at ~1.95 Å.

appreciated by inspecting the log–log plot provided as an inset in Fig. 4, left. In the short-range region ($d < 3.5$ Å), the repulsive $E^{el-prep}_{(AB)}$ rapidly becomes the dominating contributions. At the equilibrium position (~1.95 Å), such an energy term (28.89 kcal/mol) almost entirely counteracts the sum of the attractive $E^{ele}_{(AB)}$ and E^{disp} (−26.7 kcal/mol). At this position, the remaining term, i.e., the exchange–correlation energy, amounts to −7.26 kcal/mol, which is close to the overall B3LYP-D4 contribution to the interaction energy (−5.07 kcal/mol), thus providing a fundamental stabilizing component. As expected, the exchange term decays exponentially with intermolecular distance, as indicated by the linear relation in the semi-log plot shown in the inset of Fig. 4, right panel. Remarkably, our findings agree with those reported in Ref. 128 at the LED level.

To conclude this section, it is worth pointing out that in the short-range region ($d < 3.5$ Å), the log–log plot of the electrostatic interaction does not follow a linear trend (see inset in Fig. 4, left panel). As commented in Sec. II B, this is due to the fact that in this region, the dimer densities overlap and, thus, the localized fragment densities (and the associated multipoles) change as a function of the intermolecular distance. As a result, such energy terms cannot be directly compared to common EDAs, such as KM-EDA or SAPT. For this reason, in the following, we discuss the results obtained by using the KS-FEDA formulation in Eqs. (26b) and (26c).

C. A24 dataset

1. KS-FEDA in vacuo

We first start our analysis from the A24 dataset in the gas phase by considering the energetic components calculated at the KS-FEDA/aug-cc-pVTZ level of theory using B3LYP as the DFT functional. All KS-FEDA energy terms expressed in Eq. (26c) are graphically shown as a bar plot in Fig. 5 for all 24 dimers (raw data are provided in Table S17 in the supplementary material). The bars are colored according to the color palette introduced in Fig. 1 (blue: HB; green: MX; and salmon: DD).

An attractive interaction energy characterizes all dimers, except for 22–24 dimers, for which a small yet positive (~1 kcal/mol) interaction energy is obtained. Examining the different types of

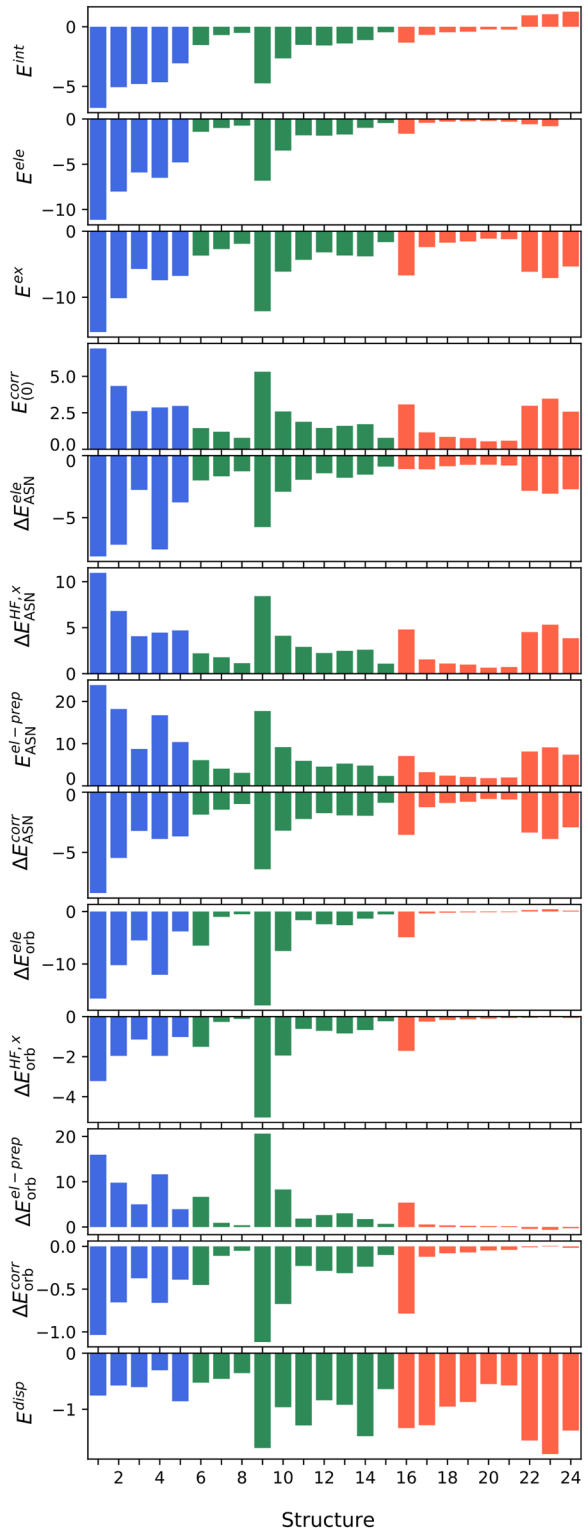

FIG. 5. KS-FEDA (B3LYP/aug-cc-pVTZ) of the A24 dataset in the gas phase [see Eq. (26c)]. All the energies are reported in kcal/mol.

interactions, HB complexes (1–5) generally display the largest interaction energies, ranging from approximately −3 to −7 kcal/mol. In contrast, DD dimers (16–24) report the lowest E^{int}, ranging from around −1.5 to 1.5 kcal/mol. As expected, MX complexes (6–15) demonstrate significant variability in interaction energies, ranging from about −5 to −0.5 kcal/mol.

The frozen interaction energy terms ($E^{ele}, E^{ex}, E^{corr}_{(0)}$) are characterized by similar trends for all dimers. In particular, electrostatic and exchange interactions are attractive, while the opposite holds for frozen correlation energy. The magnitude of the interactions varies depending on the specific complex considered. The largest and lowest absolute values of E^{ele} are reported for HB (average −6.30 kcal/mol) and DD dimers (average −0.36 kcal/mol), respectively. Some notable cases are reported for MX couples, such as formaldehyde dimer (structure 9), for which a large E^{ele} is calculated (−6.82 kcal/mol). The same trend is obtained for E^{ex} [largest and lowest absolute values reported on average for HB (−6.30 kcal/mol) and DD (−4.37 kcal/mol) respectively]. However, it should be noted that large absolute E^{ex} energies are also observed by some DD complexes, as, for instance, structures 22–24, which show a particularly low absolute E^{ele} (<0.8 kcal/mol), highlighting the role of quantum interactions. $E^{corr}_{(0)}$ almost exactly follows the same trend calculated for E^{ex}, but opposite in sign. In particular, $E^{corr}_{(0)}$ values are about half E^{ex} for all dimers, yielding a negative, attractive total DFT exchange–correlation contribution, which is obtained by summing the two terms [see Eqs. (14c) and (14d)].

We now move to the energy variations associated with the antisymmetrization of the dimer wavefunction (ASN), which can be grouped into the purely repulsive contributions E^{rep} associated with the Pauli principle [$E^{rep} = \Delta E^{HF}_{\text{ASN}}$, see Eq. (18a)] and the variation in the correlation energy (E^{corr}_{ASN}). Differently from most EDA techniques, KS-FEDA allows for dissecting E^{rep} into the electrostatic, HF exchange, and electronic preparation contributions. Such three energy terms display a similar behavior for all 24 complexes: in fact, the antisymmetrization of the total wavefunction is characterized by a stabilizing electrostatic interaction energy ($\Delta E^{ele}_{\text{ASN}}$), which is particularly significant for HB complexes (average −5.24) and also non-negligible for DD dimers (especially for structures 22–24). Similar trends, but opposite in sign, are reported for $\Delta E^{HF,x}_{\text{ASN}}$ and $E^{el-prep}_{\text{ASN}}$, for which a significant energy destabilization is obtained (up to ~24 kcal/mol for $E^{el-prep}_{\text{ASN}}$ of structure 1). The largest average absolute values of such interactions are calculated for HB complexes, following the same trend reported above for frozen terms. However, in this case, the differences between DD and MX energy components are attenuated. In fact, $\Delta E^{ele}_{\text{ASN}}$ and $\Delta E^{HF,x}_{\text{ASN}}$ average values differ by about 0.3 kcal/mol, while for $E^{el-prep}_{\text{ASN}}$, a larger, yet small, discrepancy is reported (6.33 vs 5.1 kcal/mol for MX and DD dimers, respectively). The total repulsive energy E^{rep}, given by the sum of the three terms, is almost twice the absolute values of the exchange energy computed by using the frozen energy (E^{ex}) for all dimers. In particular, their ratio ($|E^{rep}|/|E^{ex}|$) varies from an average of 1.6 for DD complexes to 1.75 for HB dimers. Their sum is thus positive and represents the so-called exchange–repulsion interaction energy, which is computed in other EDA techniques. While for HB dimers the absolute value of such energy term is almost equal (or less) to the electrostatic energy (E^{ele}), for MX and DD couples, it is larger than E^{ele} for all dimers. The last energetic contribution associated with the antisymmetrization of the dimer wavefunction is E^{corr}_{ASN}, which is attractive for all 24 complexes and follows similar trends discussed above for the other interactions. In fact, the average E^{corr}_{ASN} for HB dimers (−4.41 kcal/mol) is almost twice the average corresponding values computed for MX and DD complexes (−2.30 and −2.02 kcal/mol, respectively).

By obtaining KS-FLMOs using the SCF-converged density matrix, we access the orbital relaxation energy components, which, similar to ASN energy terms, can be grouped into HF energy components [electrostatics, HF exchange, and electronic preparation – $\Delta E^{HF}_{\text{orb}}$, see Eq. (21a)] and the orbital relaxation correlation energy (E^{corr}_{orb}). Discordantly from the energy terms discussed above, $\Delta E^{ele}_{\text{orb}}$, $\Delta E^{el-prep}_{\text{orb}}$, and $\Delta E^{corr}_{\text{orb}}$ differ in sign depending on the considered dimers, while $\Delta E^{HF,x}_{\text{orb}}$ is always negative. In particular, the sign change is associated with very low absolute energy contributions and is reported for DD dimers (structures 22–24). Indeed, for DD complexes, the orbital relaxation contributions are generally negligible, except for structure 16. The largest energy variation for all components is reported for structure 9 (MX set), followed by HB dimers. The average values of $\Delta E^{ele}_{\text{orb}}$ highly vary as a function of the dataset, ranging from −9.12 kcal/mol (HB) to −3.95 kcal/mol (MX) and 0.08 kcal/mol (DD). A similar trend, but opposite in sign, is reported for the average values of $\Delta E^{el-prep}_{\text{orb}}$ (HB: 8.84 kcal/mol; MX: 4.47 kcal/mol; DD: −0.11 kcal/mol). Generally, $\Delta E^{el-prep}_{\text{orb}}$ and $\Delta E^{ele}_{\text{orb}}$ almost counterbalance for HB and MX dimers, while for DD complexes, the former is about 50% larger than the latter (absolute value). When the two terms are summed together with $\Delta E^{HF,x}_{\text{orb}}$, the total HF relaxation energy is obtained, which is attractive for all dimers following the same trend discussed above (on average, HB: −2.08 kcal/mol; MX: −0.64 kcal/mol; DD: −0.11 kcal/mol). Finally, the correlation energy variation associated with orbital relaxation is generally negative and small, above −1 kcal/mol, except for structures 1 (−1.04 kcal/mol) and 9 (−1.12 kcal/mol).

The last KS-FEDA energy component is the dispersion energy E^{disp}, which is negative and attractive for all dimers, as expected. E^{disp} follows the opposite trend commented above for all the other energetic components. In fact, the largest and lowest absolute values are reported for DD (average: −1.12 kcal/mol) and HB dimers (average: −0.61 kcal/mol), respectively.

We finally comment on the classification proposed in Ref. 87, which has been used to classify the A24 dimers into HB, MX, and DD families. The analysis provided by KS-FEDA highlights that such partitioning of MX and DD structures should be slightly modified in light of the relative ratio between electrostatics and dispersion ($|E^{ele}|/|E^{disp}|$) terms. In particular, structure 16 (ratio = 1.2) can be assigned to the MX family (1.0 < ratio < 4.0), while structures 14 (ratio = 0.66) and 15 (ratio = 0.7) instead better belong to DD dimers for which the considered ratio is lower than 1.0. It should be noted that similar findings have also been reported in Ref. 129 based on SAPT2+3(CCD)[130]/aug-cc-pVTZ results.

2. Comparison with reference data

Among the many EDA techniques that have been proposed in the literature, SAPT has been particularly successful due to the

decomposition of the interaction energy in a few physically meaningful energy terms. In particular, within SAPT, the intermolecular interaction is treated as a perturbation to the energies of the monomers. Various SAPT methods exist depending on the truncation level of the perturbation series and the level of theory used to describe the isolated monomers.[63] Generally, the SAPT interaction energy E^{int}_{SAPT} is decomposed as[57,58,131]

$$E^{int}_{\mathrm{SAPT}} = E^{ele}_{\mathrm{SAPT}} + E^{exch}_{\mathrm{SAPT}} + E^{ind}_{\mathrm{SAPT}} + E^{disp}_{\mathrm{SAPT}}, \tag{32}$$

where E^{ele}_{SAPT} is the electrostatic energy, E^{exch}_{SAPT} is the exchange–repulsion term, E^{ind}_{SAPT} is the induction contribution, and E^{disp}_{SAPT} is the dispersion energy. Here, we focus on two SAPT variants, namely, SAPT(DFT) and SAPT2+(3)δMP2. The former is based on a DFT treatment of the monomers' electronic structure, including short-range correlation effects, while dispersion interactions are obtained by computing time-dependent DFT (TD-DFT) response functions.[59,132–137] SAPT2+(3)δMP2 is a wavefunction-based SAPT method, which introduces a more accurate treatment of electron correlation and uses HF as the reference wavefunction for monomers. SAPT(DFT) is a cost-effective EDA method that provides accurate results without introducing many terms as accurate wavefunction-based SAPT methods, such as SAPT2+(3)δMP2. The latter is selected because, when combined with the aug-cc-pVTZ basis, it is considered the "gold standard" among SAPT variants.[63]

Comparing the KS-FEDA method and SAPT requires establishing a correspondence between the energy terms expressed in Eq. (26) (reduced KS-FEDA) and Eq. (32) (SAPT). In this work, the following relationship is proposed:

$$E^{ele}_{\mathrm{SAPT}} \leftrightarrow E^{ele}, \tag{33a}$$

$$E^{exch}_{\mathrm{SAPT}} \leftrightarrow E^{ex} + E^{rep}, \tag{33b}$$

$$E^{ind}_{\mathrm{SAPT}} \leftrightarrow \Delta E^{HF}_{\mathrm{orb}}, \tag{33c}$$

$$E^{disp}_{\mathrm{SAPT}} \leftrightarrow E^{corr} + E^{disp}. \tag{33d}$$

The electrostatic terms can be directly compared, while E^{ind}_{SAPT} can be related to the HF-like energy variation due to the orbital relaxation ($\Delta E^{HF}_{\mathrm{orb}}$) proposed in KS-FEDA. As commented in Sec. IV C 1, the sum of E^{ex} and E^{rep} KS-FEDA terms represents the exchange–repulsion contribution and can thus be related to E^{exch}_{SAPT} in Eq. (32). Finally, SAPT dispersion energy can be related to the sum of KS-FEDA E^{corr} and E^{disp} to account for the correlation effects in dispersion interactions. In fact, it should be noted that dispersion energy computed by using D3 and the D4 corrections adopted here are generally smaller than the corresponding SAPT energy term[138] because part of the dispersion energy is accounted for by the correlation functional.[39]

In Fig. 6, the four SAPT(DFT) energy components (B3LYP/aug-cc-pVTZ) in Eq. (32) are correlated with the corresponding KS-FEDA (B3LYP/aug-cc-pVTZ) terms. The electrostatic component is almost equally described by the two

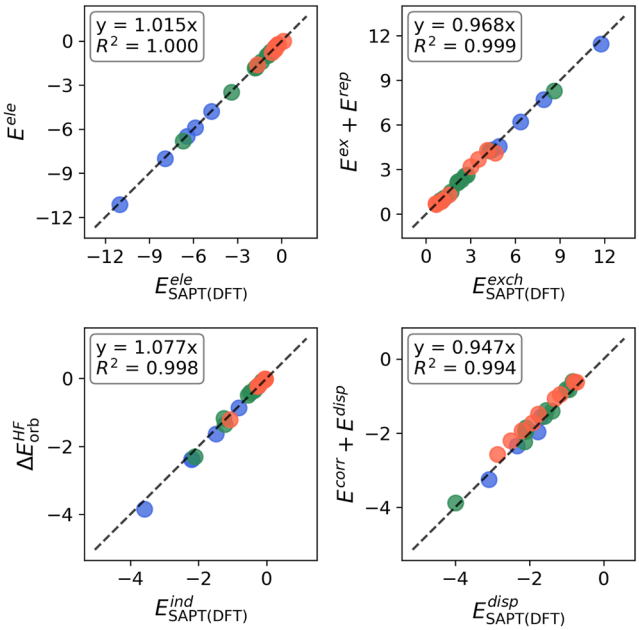

FIG. 6. Correlation plots between KS-FEDA and SAPT(DFT) energy components of the A24 dataset in the gas phase (B3LYP/aug-cc-pVTZ). All the energies are reported in kcal/mol.

methods, showing a linear coefficient and R^2 close to 1. The average and maximum discrepancies between the two approaches are, in fact, negligible, being 0.05 and 0.15 kcal/mol, respectively. Similar findings are also valid for the exchange–repulsion energy term, for which a linear coefficient and an R^2 close to 1 are obtained, reporting slightly larger differences than in the electrostatic term (−0.13 and −0.56 kcal/mol). In addition, induction and dispersion SAPT(DFT) energies well-correlate with the corresponding KS-FEDA terms. However, while for the dispersion energy, KS-FEDA predicts less attractive interaction energies, especially for MX and DD dimers (linear coefficient < 1), for induction, the opposite holds (KS-FEDA generally predicts more attractive interaction energies—on average 9%). By comparing KS-FEDA with SAPT2+(3)δMP2 reference data (see Fig. S8 in the supplementary material), such a linear fit, and in general all the correlation plots, displays an almost perfect agreement between the two methods, with all the linear coefficients between 0.97 and 1.02.

The excellent agreement between KS-FEDA and the reference SAPT2+(3)δMP2 compared to SAPT(DFT) suggests that the approaches provide different total interaction energy. To deepen this point, we compare the three approaches with the reference CCSD(T)/aug-cc-pV5(6)Z data interaction energies reported in Ref. 129. It is worth noting that the KS-FEDA interaction energy is equal to that calculated at the B3LYP-D4/aug-cc-pVTZ level of theory by definition.

In Fig. 7, the correlation plots between SAPT(DFT), SAPT2+(3)δMP2, and KS-FEDA with the reference CCSD(T) data are graphically shown. The data yield a linear dependence with $R^2 > 0.99$ for all methods. SAPT(DFT) provides a fitted

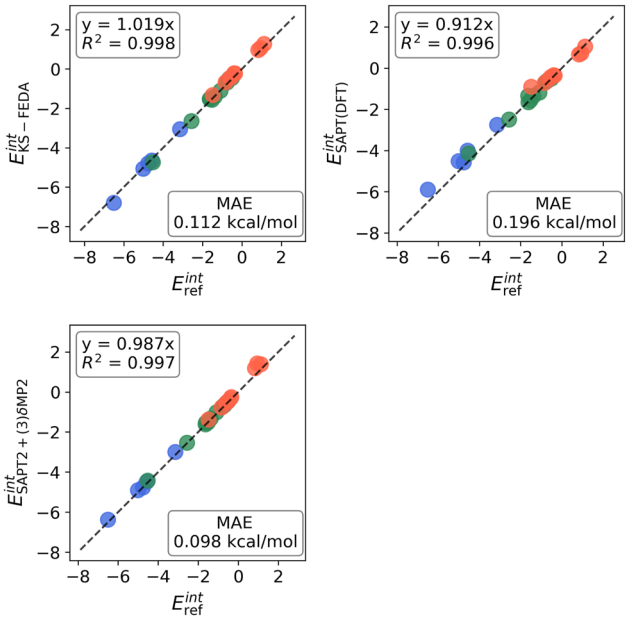

FIG. 7. Correlation plots between KS-FEDA, SAPT(DFT), SAPT2+(3)δMP2, and reference interaction [CCSD(T)/aug-cc-pV5(6)Z recovered from Ref. 129] energies of the A24 dataset in the gas phase. KS-FEDA and SAPT(DFT) energies are computed at the B3LYP/aug-cc-pVTZ. All the energies are reported in kcal/mol.

linear coefficient (0.912) and a mean absolute error (MAE = 0.196 kcal/mol), which, as expected, is the worst among the selected EDA methods. SAPT2+(3)δMP2 provides the best agreement with the reference data (MAE = 0.098 kcal/mol). However, an excellent agreement is also obtained by using KS-FEDA, but at a much lower computational cost. Finally, it should be noted that such a good agreement is preserved by performing KS-FEDA at the B3LYP/aug-cc-pVDZ. On the contrary, using such a basis set in combination with SAPT(DFT) and SAPT2+(3)δMP2 generally worsens the agreement with the reference data (see Figs. S5 and S9 in the supplementary material).

3. KS-FEDA in solution

In this work, we also introduce a description of solvent effects by means of the implicit PCM approach.[83] As stated in Sec. II C, in KS-FEDA, there are three explicit solvation contributions [see Eq. (31)], which can be summed up in a solvation interaction energy E^{solv}. Moreover, including solvent effects in the KS Fock matrix indirectly modifies all the other energy components through the variation of the solute MOs.

To analyze the effect of solvation, we graphically show in Fig. 8 the variation of the energy components defined in Eq. (30a), which are calculated as

$$\Delta E^X = E^X_{solv} - E^X_{vac}, \tag{34}$$

where E^X_{solv} and E^X_{vac} are the specific energy decomposed terms as computed in solution (water) or *in vacuo*, respectively. It should be noted that dispersion energy as computed at the D4 level is not affected by the presence of the solvent. All raw data are presented in Tables S21–S24 in the supplementary material.

The data depicted in Fig. 8 shows that the inclusion of solvent effects non-trivially affects all the energetic components, yielding an increase or a decrease in the energies depending on the specific structure. The largest total energy variation is reported by structure 9 (formaldehyde dimer), for which a large percentage variation (~35%) is also given. On average, solvent effects yield about 10% absolute variation of the total interaction energy, with the largest destabilization reported for structure 5 (ammonia dimer – 51%). As stated above, the total energy variation is due to the modification of all energetic components and the explicit solvation energy E^{solv}. While solvent effects generally make the electrostatic and correlation energies more negative, the opposite holds for the orbital relaxation terms (ΔE^{HF}_{orb}). Exchange and repulsion terms instead provide diverse trends depending on the dimer and display the opposite behavior, except for structure 3, for which both terms destabilize the interaction. The explicit contribution E^{solv} follows the same trend as the total interaction energy variation. Compared to the other energy

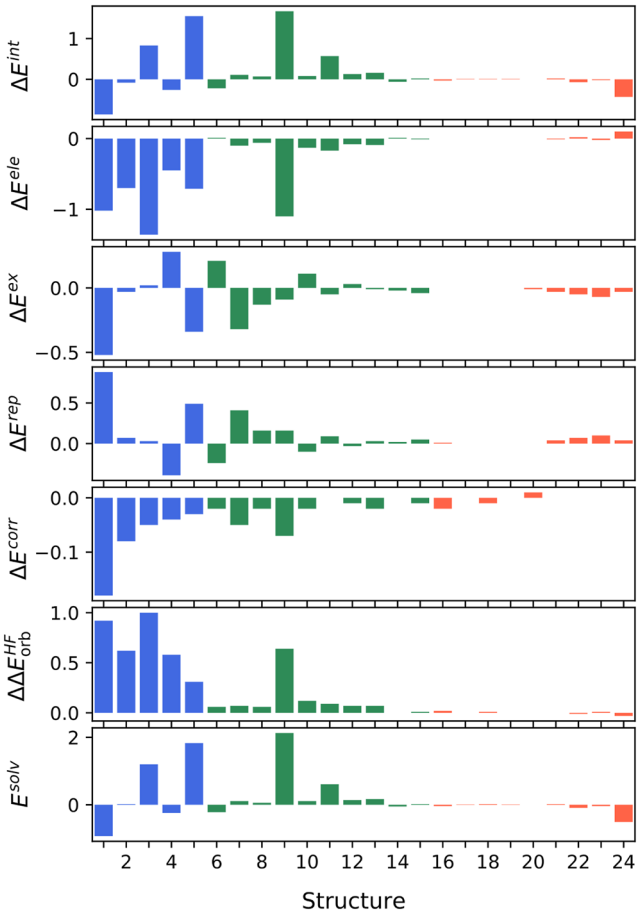

FIG. 8. KS-FEDA (B3LYP/aug-cc-pVTZ) interaction energy shifts induced by the solvent (water, ε = 78.39) of the A24 dataset [see Eq. (30a)]. All the energies are reported in kcal/mol.

terms, the largest absolute values are reported by E^{solv}, which yields a stabilization or destabilization of the dimer depending on the specific considered system. Finally, it is worth pointing out that the explicit and implicit solvent effects are generally opposite in sign, and KS-FEDA allows for an in-depth analysis of such differences in terms of the diverse energetic contributions as shown in Fig. 8.

D. S22 dataset

1. KS-FEDA in vacuo

We now move to study the S22 dataset interaction energies *in vacuo*. As for A24 dimers, all the energetic components are computed at the KS-FEDA/aug-cc-pVTZ level using the B3LYP hybrid DFT functional. All the following analyses are also performed at the PBE0/aug-cc-pVTZ, as well as by using the aug-cc-pVDZ basis set in combination with both hybrid DFT functionals (see Secs. S5–S6 in the supplementary material). In Fig. 9, all KS-FEDA energy terms [see Eq. (26c)] are graphically shown as a bar plot, colored according to the color palette introduced in Fig. 2 (blue: HB; green: MX; and salmon: DD).

An attractive interaction energy is computed for all couples. For HB complexes (1–5), the interaction energies display a significant variation, with an average value of about −14.43 kcal/mol. As expected, these complexes exhibit the most negative E^{int}, with dimer 5 (uracil dimer) reporting the lowest interaction energy (−21.40 kcal/mol). In contrast, DD dimers demonstrate considerably less negative interaction energies ranging from −0.41 kcal/mol (structure 8) to −12.51 kcal/mol (structure 15), averaging around −4.92 kcal/mol, while for MX complexes, the highest average E^{int} is reported (−3.72 kcal/mol).

By first considering the frozen energy components, for HB complexes, E^{ele} is highly variable (from −4.95 to −33.27 kcal/mol) and averages at ∼−22.45 kcal/mol, indicating strong attractive forces, as expected considering the HB character of the intermolecular interaction. The exchange energy E^{ex} for these complexes shows generally larger absolute values, averaging at about −31.86 kcal/mol, remarkably reflecting the significant covalent contribution at short distances for HB interactions. The correlation energy $E^{corr}_{(0)}$ is instead repulsive (average of 15.02 kcal/mol) for all HB dimers. DD complexes, in contrast, report an average E^{ele} of −4.18 kcal/mol, reflecting the overall weaker electrostatic interactions compared to HB dimers, although some notable exceptions are reported (structure 13 and 15). Similarly, the exchange and correlation energies are also significantly smaller (in absolute value), averaging at about −13.05 and 6.06 kcal/mol, respectively. However, while for HB complexes, E^{ex} is 40% larger than E^{ele}, for DD dimers; E^{ex} is significantly larger (up to ∼500% for structure 8). MX complexes exhibit the smallest absolute values for the frozen components: the average electrostatic energy, E^{ele}, is −3.50 kcal/mol, and E^{ex} averages at −7.70 kcal/mol, while correlation energy at 3.47 kcal/mol.

The analysis of ASN contributions reveals an overall significant repulsive energy, particularly noticeable in HB complexes resulting from a delicate balance between interactions of different natures. The average $\Delta E^{ele}_{\text{ASN}}$ for HB dimers is stabilizing (average −15.31 kcal/mol), as well for DD and MX complexes (average −5.94 and −3.71 kcal/mol, respectively). Similarly, the average $\Delta E^{corr}_{\text{ASN}}$ for HB complexes stabilizes the interaction (average −17.72 kcal/mol), substantially more attractive than those observed for DD (−6.81

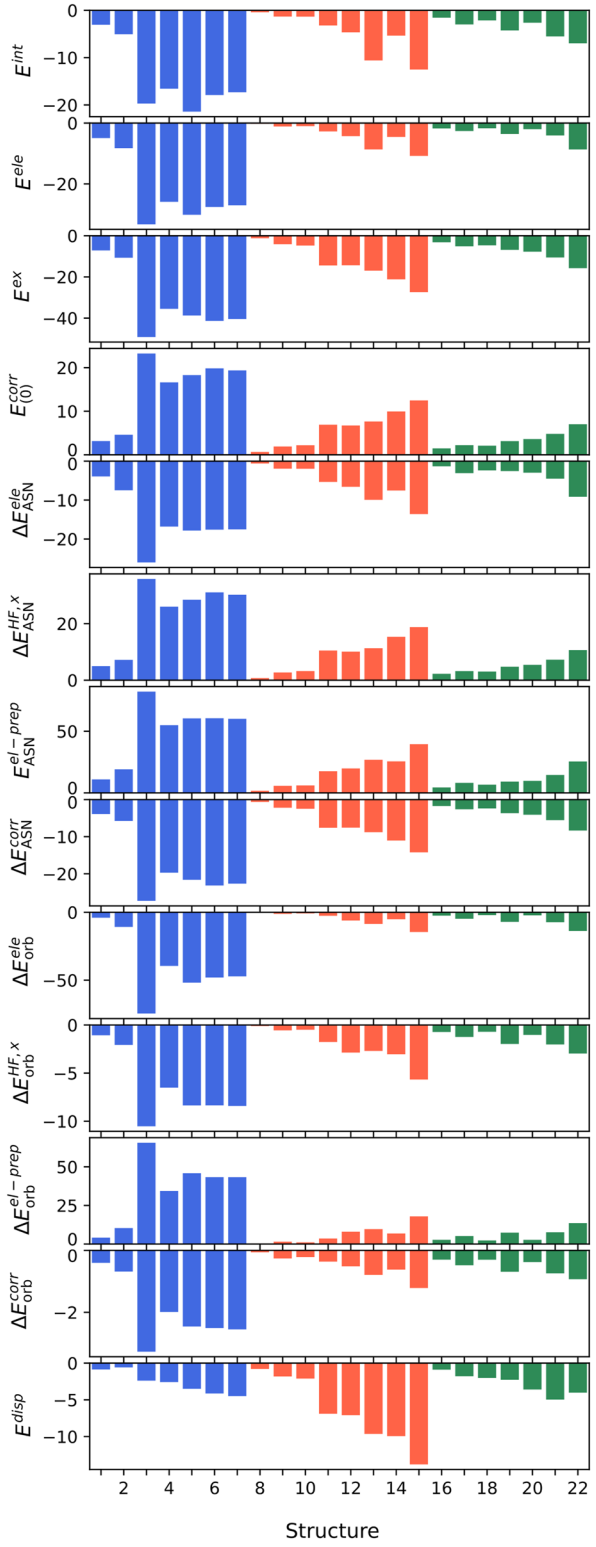

FIG. 9. KS-FEDA (B3LYP/aug-cc-pVTZ) of the S22 dataset in the gas phase [see Eq. (26c)]. All the energies are reported in kcal/mol.

kcal/mol) and MX (−4.05 kcal/mol) dimers, reflecting the stronger electrostatic interactions and correlation readjustments occurring in HB complexes as a consequence of the antisymmetrization of the total wavefunction. In contrast, HF exchange and electronic preparation contributions to the ASN energy variation are destabilizing for all complexes. In addition, in this case, HB dimers report the most destabilizing interaction energy components (on average, 49.74 and 23.40 kcal/mol for $\Delta E^{corr}_{\mathrm{ASN}}$ and $E^{HF,x}_{\mathrm{ASN}}$, respectively). We remark that the ASN energy contributions associated with the Pauli repulsion principle can be grouped into the purely repulsive term $E^{rep} = \Delta E^{HF}_{\mathrm{ASN}}$, which is large for all dimers (especially HB, for which it reaches 91.46 kcal/mol) and follows the same trend described above for $E^{el-prep}_{\mathrm{ASN}}$. Such huge repulsive interactions highlight the substantial electronic reorganization associated with the studied dimers upon imposing antisymmetry.

The total contribution arising from orbital relaxation energy components stabilizes the interaction in all S22 dimers, highlighting the attractive forces resulting from electronic structural relaxations. HB complexes demonstrate significant variations, with an average $\Delta E^{ele}_{\mathrm{orb}}$ of −39.41 kcal/mol, while for DD and MX dimers, such an energetic component is almost one order of magnitude lower on average (−4.88 and −5.67 kcal/mol, respectively). In this case, both $\Delta E^{HF,x}_{\mathrm{orb}}$ and $\Delta E^{corr}_{\mathrm{orb}}$ are attractive and stabilize the dimer interaction. While for DD and MX complexes, their magnitude is comparable with the electrostatic relaxation term, for HB couples, they are much lower in absolute value (−6.47 and −1.98 kcal/mol on average). This indicates that HB interactions, compared to the other dimers, are generally characterized by a substantial lowering of the electrostatic energy upon relaxation of the electronic structure of the dimer. The electronic preparation component, $\Delta E^{el-prep}_{\mathrm{orb}}$ is positive for all dimers, taking into account the energy spent to bring the monomers from the ASN electronic configuration to the fully optimized electronic structure. HB complexes require significant average reorganization energy of 35.26 kcal/mol, whereas DD and MX dimers need less energy on average (5.91 kcal/mol). The energy variation in electrostatics, HF-exchange, and electronic preparation summed together represent $\Delta E^{HF}_{\mathrm{orb}}$ [see Eq. (21a)], which is attractive for all dimers. For HB complexes, such an energy term is generally large in absolute value (average −10.62 kcal/mol), especially for structure 3 (urea dimer: −19.53 kcal/mol). For both DD and MX dimers, it is instead much smaller (in absolute value), on average −0.93 and −1.28 kcal/mol, respectively, coherently with the different nature of the interactions involved.

To end the discussion, we move to the dispersion energy term. For HB complexes, the dispersion energy generally shows small absolute values, averaging around −2.65 kcal/mol. Such a finding indicates that while dispersion forces contribute to the overall stability, they play a less dominant role compared to the stronger electrostatic and bonding forces prevalent in these complexes. In contrast, DD complexes exhibit significantly higher average dispersion energies, around −6.51 kcal/mol. MX complexes display intermediate dispersion energy values, averaging −2.79 kcal/mol. This indicates a balanced contribution from dispersion alongside other stabilizing forces, reflecting the hybrid nature of their interactions.

We finally remark that in the present study, we have used the assignment in HB, MX, and DD couples provided in Ref. 88. However, similar to the A24 dataset, also in this case, the KS-FEDA decomposition suggests that the definition of the MX and DD groups should be modified by considering the ratio between electrostatics and dispersion ($|E^{ele}|/|E^{disp}|$). In particular, if the dimers that are characterized by a ratio lower than 0.75 are assigned to the DD group, structures 13 (uracil dimer) and 15 (adenine-thymine) should be moved to the MX subset, while the T-shaped benzene dimer (structure 20) should be moved to DD one. This is in agreement with the SAPT2+(3)/aug-cc-pVTZ findings.[58]

2. Comparison with reference data

In this section, we first assess the KS-FEDA quality by comparing with SAPT(DFT) and SAPT2+(3)δMP2 levels variants for the S22 dataset, by using the same assignment in Eq. (33).

In Fig. 10, the four SAPT(DFT) energy components (B3LYP/aug-cc-pVTZ) in Eq. (32) are correlated to the corresponding KS-FEDA (B3LYP/aug-cc-pVTZ) terms (also see Sec. S6.2 in the supplementary material). The electrostatic component is almost equally described by the two methods, showing an R^2 equal to 1 and a fitted linear coefficient close to 1 (1.003). The average and maximum discrepancies between the two approaches are, in fact, negligible, being 0.03 and 0.27 kcal/mol, respectively. For the exchange–repulsion energy term, an R^2 close to 1 is obtained, while the linear coefficient is about 0.96, showing that KS-FEDA predicts smaller repulsive interactions. The discrepancies between the two methods are in this case larger than in the electrostatic term. In fact, the average difference is 0.69 kcal/mol, displaying a maximum deviation for structure 5 of about 2.02 kcal/mol. On average, KS-FEDA repulsive interactions are 7% larger than those computed at the SAPT(DFT) level.

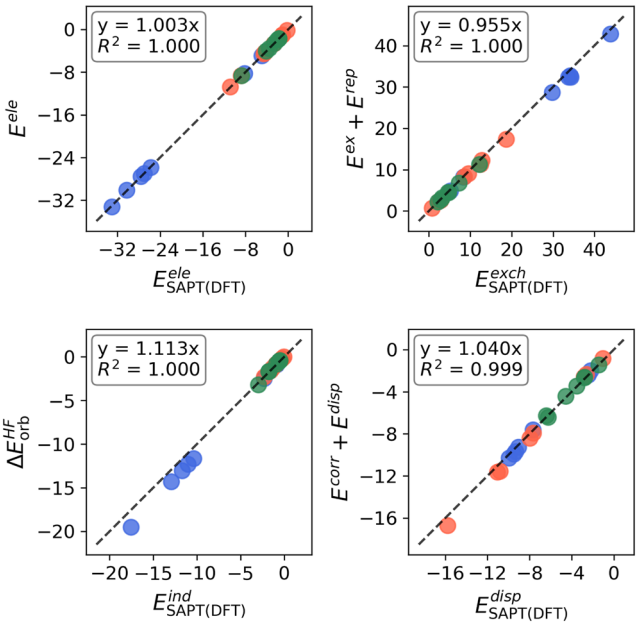

FIG. 10. Correlation plots between KS-FEDA and SAPT(DFT) energy components of the S22 dataset in the gas phase (B3LYP/aug-cc-pVTZ). All the energies are reported in kcal/mol.

Induction and dispersion SAPT(DFT) energies also well-correlate with the corresponding KS-FEDA terms ($R^2 > 0.99$). As also reported for the A24 dataset, for induction, KS-FEDA generally predicts more attractive, interaction energies, especially for the HB dimers (1–7) (on average 9%). The agreement for the dispersion energy component is in this case similar to that reported for the frozen terms: KS-FEDA predicts more attractive interaction energies, especially for DD complexes (on average 5%, −0.28 kcal/mol).

By comparing KS-FEDA with SAPT2+(3)δMP2 reference data (see Fig. S17 in the supplementary material), the linear fit, and in general all the correlation plots, displays a general better agreement between the two methods, with all the linear coefficients between 0.95 (dispersion) and 1.08 (induction).

We finally compare the total interaction energies as computed at the KS-FEDA, SAPT(DFT), and SAPT2+(3)δMP2 levels with the reference best estimate interaction energies reported in Ref. 139. As for the A24 dataset, we remark that the KS-FEDA interaction energy corresponds to that computed at the B3LYP-D4/aug-cc-pVTZ level.

In Fig. 11, the correlation plots between the various EDA techniques and the reference CCSD(T) data are shown. For all methods, we report a linear dependence with $R^2 > 0.99$. Similar to A24, SAPT(DFT) yields the worst fitted linear coefficient (0.860) and a mean absolute error (MAE = 0.968 kcal/mol), while the SAPT2+(3)δMP2 method yields the best agreement with the reference data (MAE = 0.161 kcal/mol). For KS-FEDA, an MAE of about 0.4 kcal/mol is computed, highlighting the overall good performance of the DFT-D4 method, at a much lower computational cost than SAPT techniques. It is also worth remarking that for the S22 dataset, the computed KS-FEDA MAE and trend are consistently produced by changing the DFT functional (PBE0) or the basis set (aug-cc-pVDZ), demonstrating the method stability. It should be noted that the same trend is not reported by SAPT methodologies, for which the change in the basis set or DFT functional, for SAPT(DFT), generally deteriorates the agreement with the reference data (see Secs. S5–S6 in the supplementary material).

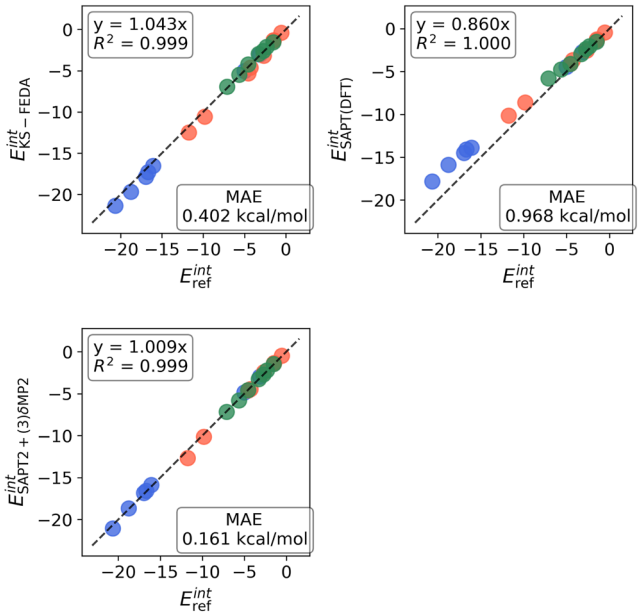

FIG. 11. Correlation plots between KS-FEDA, SAPT(DFT), SAPT2+(3)δMP2, and reference interaction energies (recovered from Ref. 139) of the S22 dataset in the gas phase. KS-FEDA and SAPT(DFT) energies are computed at the B3LYP/aug-cc-pVTZ. All the energies are reported in kcal/mol.

3. KS-FEDA in solution

In this section, we study how solvent effects, as modeled by the implicit PCM model, affect the interaction energy components of the S22 as solvated in water. As for the A24 dataset, in Fig. 12, the interaction energy shifts [see Eq. (34)] for the energy components defined in Eq. (30a) are graphically shown for all S22 dimers. All raw data are presented in Tables S47–S50 in the supplementary material.

The data presented in Fig. 12 shows that including solvent effects significantly influences all energetic components, resulting in

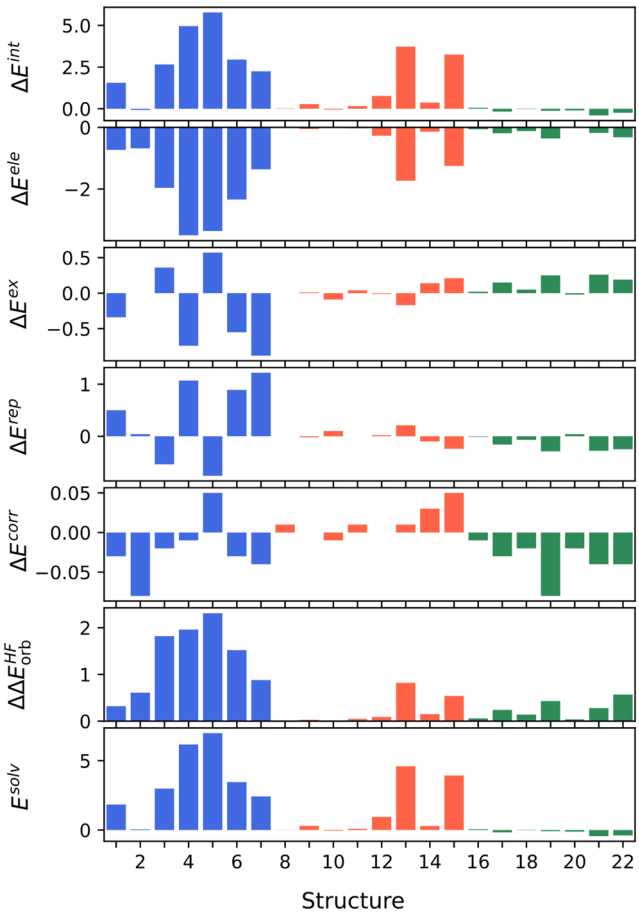

FIG. 12. KS-FEDA (B3LYP/aug-cc-pVTZ) interaction energy shifts induced by the solvent (water, $\varepsilon = 78.39$) of the S22 dataset [see Eq. (30a)]. All the energies are reported in kcal/mol.

either an increase or decrease in the energies, depending on the specific molecular structure. The most substantial total energy change of about 5.8 kcal/mol is reported in structure 5 (uracil dimer), which also exhibits a considerable percentage change of about 30%. Similar to the A24 dataset, solvent effects, on average, lead to a 13% absolute change in the total interaction energy, with the largest destabilization occurring for structure 1 (ammonia dimer – 51%).

The total energy change arises from variations in all energetic components coupled with the explicit solvation energy E^{solv}. Typically, solvent effects tend to make the electrostatic and correlation energies more negative, whereas they have the opposite effect on the orbital relaxation terms ($\Delta E^{HF}_{\text{orb}}$). The exchange and repulsion terms show varying trends across different dimers, generally exhibiting opposite behaviors. The explicit contribution E^{solv} directly resembles the trend depicted for the total interaction energy variation. Indeed, as for the A24 dataset, E^{solv} records the largest absolute values among the various energy terms, leading to a destabilization of the dimer in HB and DD complexes, while it tends to stabilize MX complexes. Interestingly, E^{solv} is mainly determined by $E^{solv}_{(0)}$, while ASN and relaxation solvation terms [see Eq. (30b)] are generally substantially lower in absolute value (see Secs. S5 and S6 in the supplementary material). Remarkably, KS-FEDA provides a detailed examination of these variations, highlighting that explicit and implicit solvent effects are typically opposite in sign, non-trivially affecting the interaction energies as shown in Fig. 12.

E. Ionic hydrogen bondend systems: IHB15 dataset

1. KS-FEDA in vacuo

We now move to study the IHB15 dataset interaction energies in the gas phase. As for A24 and S22 dimers, all the energetic components are computed at the KS-FEDA/aug-cc-pVTZ level using the B3LYP hybrid DFT functional. All the following analyses are also performed at the PBE0/aug-cc-pVTZ, exploiting the aug-cc-pVDZ basis set in combination with both hybrid DFT functionals (see Secs. S7–S8 in the supplementary material). In Fig. 13, all the KS-FEDA energy terms [see Eq. (26c)] are graphically shown as a bar plot, colored according to the palette introduced in Fig. 3 (salmon: anions and blue: cations).

An attractive, large interaction energy (E^{int}) is computed for all complexes. For anionic dimers (1–3), E^{int} varies between −11.64 and −21.10 kcal/mol, with an average value of about −17.64 kcal/mol. Cationic complexes (4–15) display a wider range of interaction energies, from −16.94 kcal/mol (structure 11) to −29.94 kcal/mol (structure 13), with an average interaction energy of −20.66 kcal/mol. Overall, the computed E^{int} values for IHB15 dimers are substantially larger than those computed for A24 and S22 dimers, highlighting the different nature of the non-covalent interactions characterizing this dataset.

To deepen into the nature of the interactions, we first consider the frozen energy components. For complexes 1–3, E^{ele} varies significantly (from −13.11 to −28.21 kcal/mol) and averages at −22.29 kcal/mol, indicating strong attractive electrostatic forces. The exchange energy E^{ex} for anions has larger absolute values, averaging at −27.32 kcal/mol, reflecting significant covalent contributions at equilibrium distances. For all anions, exchange energy is larger than electrostatics (in absolute values). As also reported for both

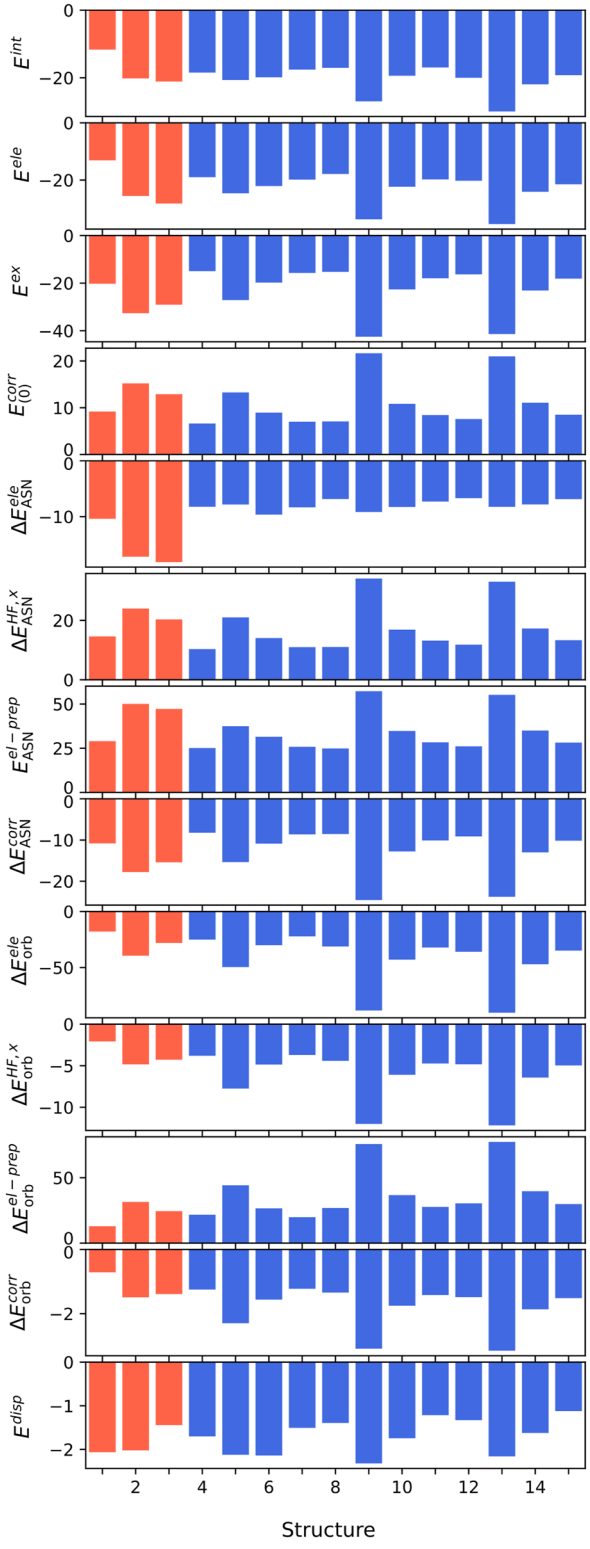

FIG. 13. KS-FEDA (B3LYP/aug-cc-pVTZ) of the IHB15 dataset in the gas phase [see Eq. (26c)]. All the energies are reported in kcal/mol.

A24 and S22, the frozen correlation energy $E^{corr}_{(0)}$ is repulsive for all dimers, averaging at about 12.42 kcal/mol for complexes 1–3. Cationic dimers (4–15) report an average E^{ele} of −23.37 kcal/mol, reflecting generally larger attractive electrostatic interactions compared to anions (1–3). The exchange and correlation energies in complexes 4–15 are instead smaller (in absolute value), averaging −22.90 and 11.00 kcal/mol, respectively. While for complexes 1–3, E^{ex} overcomes E^{ele} (in absolute value – up to 55% for structure 1), for complexes 4–15, E^{ex} is generally less stabilizing, except for structures 5, 9, 13 (ions interacting with $MeNH_2$), and 10, for which the two interactions are almost equivalent.

Analysis of ASN contributions reveals significant repulsive energy, resulting from a delicate balance between interactions of diverse natures. The average ΔE^{ele}_{ASN} for complexes 1–3 is stabilizing (average −15.23 kcal/mol), as is the case for complexes 4–15 (average −7.93 kcal/mol). The correlation contribution ΔE^{corr}_{ASN} stabilizes the interaction with a similar extent (average −14.66 and −12.92 kcal/mol for the anions and cations, respectively). In contrast, HF exchange and electronic preparation contributions to the ASN energy variation act as destabilizing terms for all complexes. As expected, $E^{el-prep}_{ASN}$ represents the most destabilizing interaction energy component, which accounts, on average, 42.10 and 34.13 kcal/mol for the two subsets, respectively. The sum of the two destabilizing energy terms and the electrostatic variation results in the ASN energy contributions associated with the Pauli repulsion [$E^{rep} = \Delta E^{HF}_{ASN}$; see Eq. (18a)]. Such energy term is large for all complexes (on average 44.07 kcal/mol), reaching the maximum for dimer 9 (82.16 kcal/mol). Such huge repulsive interactions highlight the substantial electronic reorganization associated with the studied complexes upon imposing antisymmetry.

Opposite to the destabilization provided by the antisymmetrization, the total contribution arising from orbital relaxation energy components stabilizes the interaction in all complexes. This again arises from a delicate balance between the various interactions, the most substantial being electrostatic, followed by the electronic preparation, exchange, and finally correlation. Anionic complexes (1–3) demonstrate significant inductive contributions (average ΔE^{ele}_{orb} −28.15 kcal/mol); for cationic complexes 4–15, such an energetic component is even more stabilizing (on average −44.13 kcal/mol). In addition, $\Delta E^{HF,x}_{orb}$ and ΔE^{corr}_{orb} are attractive and stabilize the complex interaction. For all complexes, their magnitude is considerably lower in absolute value with respect to the electrostatic relaxation term by almost one order of magnitude (−5.80 and −1.70 kcal/mol on average, respectively). The electronic preparation component, $\Delta E^{el-prep}_{orb}$, accounting for the energy spent to bring the monomers from the ASN electronic configuration to the fully optimized electronic structure, destabilizes the interaction for all complexes. Its magnitude is comparable with the electrostatic variation (on average, 22.94 and 38.05 kcal/mol for anions and cations, respectively). The energy variation in electrostatics, HF-exchange, and electronic preparation summed together represent ΔE^{HF}_{orb}, which is attractive for all complexes, stabilizing the interaction of about −11.77 kcal/mol on average.

To conclude, we consider the dispersion energy term. For all dimers, E^{disp} displays small absolute values, ranging from −1.12 to −2.32 kcal/mol. This indicates that while dispersion forces contribute to the overall stability, they play a less dominant role in determining the global interaction energy contributing by less than 9% on average. For both anionic and cationic dimers, the importance of electrostatic, exchange, and orbital relaxation terms compared to dispersion energy confirms the HB nature of the considered dimers.

2. Comparison with reference data

In this section, we first assess the KS-FEDA quality by comparing it with the SAPT2+(3)δMP2 variant for the IHB15 dataset, by using the same assignment in Eq. (33).

In Fig. 14, the four SAPT2+(3)δMP2 energy components in Eq. (32) are correlated with the corresponding KS-FEDA (B3LYP/aug-cc-pVTZ) terms (also see Sec. S8.2 in the supplementary material). The electrostatic component is almost equally described by the two methods, showing an R^2 and a fitted linear coefficient close to 1, with an average discrepancy between the two approaches of just −0.04 kcal/mol. For the exchange–repulsion energy term, an R^2 close to 1 is obtained, while the linear coefficient is about 1.010, showing again the good agreement between the two methods. KS-FEDA generally predicts repulsive interactions slightly larger than those computed at the SAPT2+(3)δMP2 level (on average, 0.13 kcal/mol).

Induction SAPT2+(3)δMP2 energies also well-correlate with the corresponding KS-FEDA terms ($R^2 > 0.99$). As reported for the A24 and S22 datasets, KS-FEDA induction energies are more attractive (about 3%). The fitted linear coefficient for dispersion contributions is lower than that computed for the induction term (1.033 vs 1.040). However, the qualitative agreement for the IHB15 dataset is less satisfactory compared to that obtained for A24 and S22. It is, in fact, worth noting that KS-FEDA dispersive interactions are generally less attractive than the reference (0.89 kcal/mol on average) for

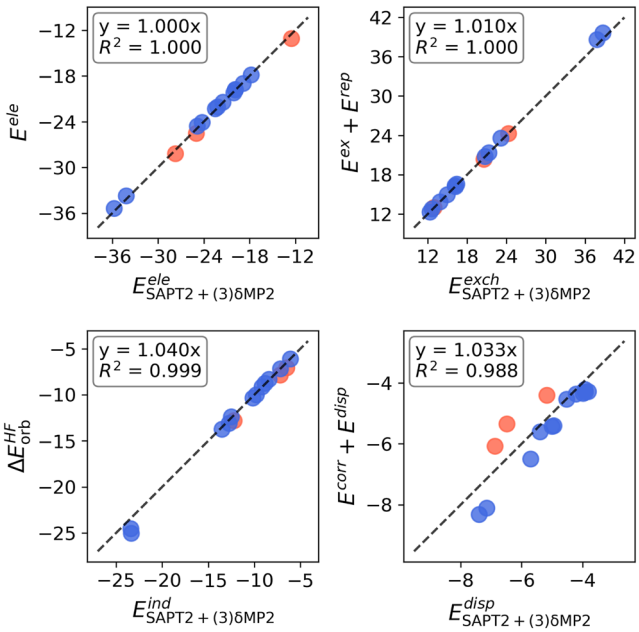

FIG. 14. Correlation plots between KS-FEDA (B3LYP/aug-cc-pVTZ) and SAPT2+(3)δMP2 energy components of the IHB15 dataset in the gas phase. All the energies are reported in kcal/mol.

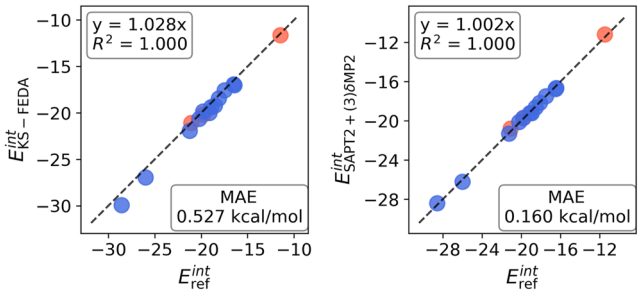

FIG. 15. Correlation plots between KS-FEDA, SAPT2+(3)δMP2, and reference interaction energies (recovered from Ref. 89) of the IHB15 dataset in the gas phase. KS-FEDA energies are computed at the B3LYP/aug-cc-pVTZ. All the energies are reported in kcal/mol.

anion complexes, while the opposite holds for the cationic dimers (−0.46 kcal/mol on average).

We finally compare the total interaction energies, as computed at the KS-FEDA and SAPT2+(3)δMP2, to the reference CCSD(T)/complete basis set (CBS) interaction energies reported in Ref. 89. We remark once again that KS-FEDA interaction energy corresponds to that computed at the B3LYP-D4/aug-cc-pVTZ level.

In Fig. 15, the correlation plots between the two EDA techniques and the reference CCSD(T) data are shown. For both methods, we report a linear dependence with $R^2 \sim 0.99$. Similar to A24 and S22, the SAPT2+(3)δMP2 method yields the best agreement with the reference data (MAE = 0.160 kcal/mol). For KS-FEDA, an MAE of about 0.5 kcal/mol is computed, highlighting the overall good performance of the DFT-D4 method. It is worth remarking that also for the IHB15 dataset, the computed KS-FEDA MAE and trend are consistently produced by changing the DFT functional (PBE0) or the basis set (aug-cc-pVDZ), demonstrating the method stability (see Secs. S7–S8 in the supplementary material). Such results show that KS-FEDA has the potential to be applied to complex cases, such as ionic HB complexes.

3. KS-FEDA in solution

We finally investigate solvent effects on the interaction energy components of the IHB15 as solvated in water. As for the A24 and S22 datasets, shown in Fig. 16, the interaction energy shifts [see Eq. (34)] for the energy components defined in Eq. (30a) are graphically depicted for all IHB15 dimers. All raw data are presented in Tables S69–S72 in the supplementary material.

Figure 16 shows that solvent effects substantially affect all energetic components, resulting in an overall destabilization of the global interaction energies for all ionic dimers. This is in agreement with what has been previously reported for HB dimers in A24 and S22 datasets. The largest energy variation of about 10.6 kcal/mol is reported in structure 12, which also exhibits the largest percentage change of about 53%. On average, solvent effects destabilize the non-covalent interactions by about 38%, reporting the most considerable variation compared to the other two datasets. This indeed highlights how solvent effects can crucially determine the interaction between ionic species.

To deepen the analysis, we investigate how solvent effects influence the energetic components. For all dimers, solvation enhances electrostatic interactions as calculated *in vacuo*, which become more attractive for all dimers, with a contribution ranging from −0.58 to −2.53 kcal/mol. Interestingly, depending on the charge of the ionic dimers, exchange and repulsion terms behave in an opposite way. For instance, for anionic complex, E^{ex} increases, while E^{rep} decreases. Solvent effects act in the opposite direction also for the exchange–repulsion term, given by the sum of the two contributions, stabilizing or destabilizing the non-covalent interaction for anions (1–3) and cations (4–15), respectively. A similar outcome is also reported for the influence on correlation energy, for which, however, the anionic complex 1 displays a destabilizing contribution. For all dimers, instead, solvent effects destabilize the orbital relaxation terms (ΔE^{HF}_{orb}) interaction energy.

The global variation provided by summing all the energetic terms is generally small in absolute value, varying from −0.31 to 0.47 kcal/mol. Finally, as reported for both A24 and S22 datasets, E^{solv} shows the largest values among the various energy terms, leading to a destabilization of all dimers, correlating particularly well with the total energy variation ΔE^{int}. Interestingly, while for A24 and S22 dimers, E^{solv} is mainly determined by the frozen contribution, for IHB15 complexes, a large contribution (on average, 21.42%) of ΔE^{solv}_{orb} is reported. This again highlights the different nature

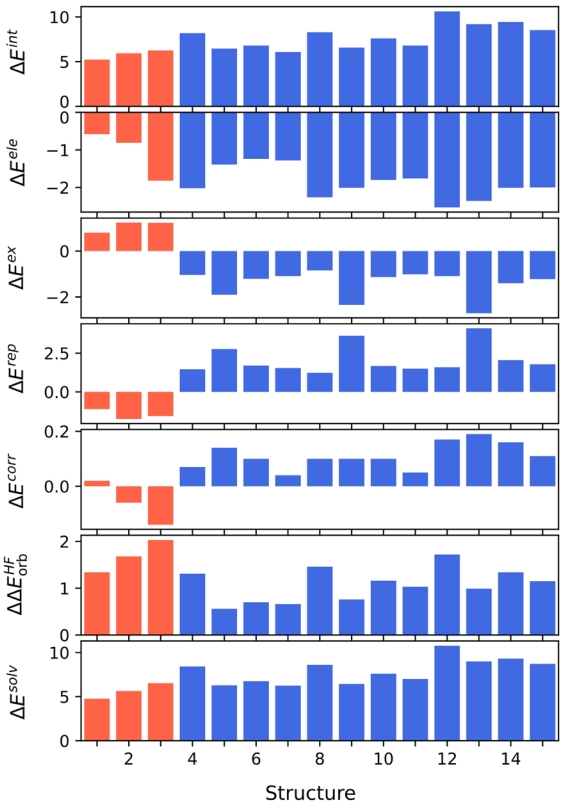

FIG. 16. KS-FEDA (B3LYP/aug-cc-pVTZ) interaction energy shifts induced by the solvent (water, ε = 78.39) of the IHB15 dataset [see Eq. (30a)]. All the energies are reported in kcal/mol.

of the interactions governing the electronic structure of the ionic complexes.

V. SUMMARY AND CONCLUSIONS

We have introduced the Kohn–Sham fragment energy decomposition analysis (KS-FEDA), which is a novel EDA technique based on the developed KS-FLMOs. FLMOs are obtained through a variational minimization of the local energies of the fragments constituting a molecular system. This is equivalent to maximizing their electronic repulsion energy: as a consequence, FLMOs are maximally localized in the pre-defined fragment regions. In the resulting KS-FEDA, the interaction energy is decomposed into electrostatics, exchange, and correlation. Dispersion has been considered by employing empirical corrections (such as the D4 model); however, the approach is general and can be coupled with more sophisticated methods and non-local approaches. To validate our method, we study the dependence of KS-FEDA(LED) energy contributions on the basis set and DFT functional, as well as the decay of the energetic contributions as a function of the intermolecular distance for a water dimer. Detailed assessments on the KS-FEDA dependence on the DFT functionals will be the topic of future communications.

The energy contributions of KS-FEDA(LED) are further dissected into frozen, antisymmetry, and orbital relaxation contributions, permitting to analyze the interactions between unperturbed, antisymmetrized, and self-consistently relaxed densities. This not only provides novel physical insights into the intermolecular interactions but also facilitates the comparison with traditional EDA techniques. In this paper, this is demonstrated by comparing the final KS-FEDA energetic components with SAPT methods, based on DFT—SAPT(DFT)—or wavefunction theory—SAPT2+(3)δMP2—for two datasets (A24 and S22) that are widely exploited for non-covalent interactions. The method has also been challenged to calculate the intermolecular interactions of ionic hydrogen bonding dimers (IHB15 dataset), showing the potential to study such systems. By properly comparing the energetic components, a very good agreement between KS-FEDA and the golden standard SAPT2+(3)δMP2 is reported for all datasets, demonstrating the validity and robustness of the developed approach. It is worth remarking that SAPT dispersion interactions have been compared to the sum of KS-FEDA correlation and dispersion terms. To further dissect correlation and dispersion terms in KS-FEDA, the definition of a suitable dispersionless functional, as proposed in Ref. 103, would be ideal. Such an aspect will be investigated in future communications. Furthermore, the extension to analyze non-covalent interactions in solution, as modeled by using the PCM approach, highlights the versatility of our method, allowing for studying both direct and indirect solvent effects on intermolecular interactions.

To conclude, KS-FLMOs and KS-FEDA have been applied to non-covalently interacting molecular systems. However, the developed theory is general enough to also be applied to covalently bonded fragments, differently from perturbation-based EDA methods. Furthermore, the developed KS-FLMOs can be potentially exploited for diverse applications other than KS-FEDA, ranging from reactive chemistry and spectroscopy to studying local phenomena taking place *in vacuo* or solution, possibly described at the atomistic level in a polarizable QM/MM fashion.[140]

SUPPLEMENTARY MATERIAL

The supplementary material encompasses the computational protocol; raw data for Figs. 1–16; and additional raw data for KS-FEDA (B3LYP/aug-cc-pVDZ, PBE0/aug-cc-pVDZ, PBE0/aug-cc-pVTZ) and SAPT(DFT) (B3LYP/aug-cc-pVDZ, PBE0/aug-cc-pVDZ, PBE0/aug-cc-pVTZ).

ACKNOWLEDGMENTS

This work was funded by the European Union – Next Generation EU in the framework of the PRIN 2022 PNRR project POSEIDON – Code P2022J9C3R. This publication is also based upon work of COST Action CA21101 "Confined molecular systems: from a new generation of materials to the stars" (COSY) supported by COST (European Cooperation in Science and Technology). The author thanks Piero Lafiosca (SNS) for useful comments on the manuscript. The author also acknowledges Chiara Cappelli (SNS) for computer resources and the Center for High-Performance Computing (CHPC) at SNS for providing the computational infrastructure.

AUTHOR DECLARATIONS

Conflict of Interest

The author has no conflicts to disclose.

Author Contributions

Tommaso Giovannini: Conceptualization (equal); Data curation (equal); Formal analysis (equal); Funding acquisition (equal); Investigation (equal); Methodology (equal); Project administration (equal); Resources (equal); Software (equal); Supervision (equal); Validation (equal); Visualization (equal); Writing – original draft (equal); Writing – review & editing (equal).

DATA AVAILABILITY

The data that support the findings of this study are available from the corresponding author upon reasonable request.

REFERENCES

[1] A. Stone, *The Theory of Intermolecular Forces* (Oxford University Press, Oxford, 2013).
[2] D. Leckband and J. Israelachvili, "Intermolecular forces in biology," Q. Rev. Biophys. **34**, 105–267 (2001).
[3] V. T. Moy, E.-L. Florin, and H. E. Gaub, "Intermolecular forces and energies between ligands and receptors," Science **266**, 257–259 (1994).
[4] E. H. Krenske and K. Houk, "Aromatic interactions as control elements in stereoselective organic reactions," Acc. Chem. Res. **46**, 979–989 (2013).
[5] B. Mennucci and S. Corni, "Multiscale modelling of photoinduced processes in composite systems," Nat. Rev. Chem. **3**, 315–330 (2019).
[6] B. Mennucci, "Modeling environment effects on spectroscopies through QM/classical models," Phys. Chem. Chem. Phys. **15**, 6583–6594 (2013).

[7]J. G. Pedreira, L. S. Franco, and E. J. Barreiro, "Chemical intuition in drug design and discovery," Curr. Top. Med. Chem. **19**, 1679–1693 (2019).
[8]T. Giovannini, F. Egidi, and C. Cappelli, "Molecular spectroscopy of aqueous solutions: A theoretical perspective," Chem. Soc. Rev. **49**, 5664–5677 (2020).
[9]T. Giovannini, F. Egidi, and C. Cappelli, "Theory and algorithms for chiroptical properties and spectroscopies of aqueous systems," Phys. Chem. Chem. Phys. **22**, 22864–22879 (2020).
[10]C. Hampel and H.-J. Werner, "Local treatment of electron correlation in coupled cluster theory," J. Chem. Phys. **104**, 6286–6297 (1996).
[11]C. Riplinger, B. Sandhoefer, A. Hansen, and F. Neese, "Natural triple excitations in local coupled cluster calculations with pair natural orbitals," J. Chem. Phys. **139**, 134101 (2013).
[12]R. M. Parrish and C. D. Sherrill, "Quantum-mechanical evaluation of π–π versus substituent-π interactions in π stacking: Direct evidence for the Wheeler–Houk picture," J. Am. Chem. Soc. **136**, 17386–17389 (2014).
[13]Q. Ma and H.-J. Werner, "Explicitly correlated local coupled-cluster methods using pair natural orbitals," Wiley Interdiscip. Rev.: Comput. Mol. Sci. **8**, e1371 (2018).
[14]S. Saebo and P. Pulay, "Local treatment of electron correlation," Annu. Rev. Phys. Chem. **44**, 213–236 (1993).
[15]S. Gómez, T. Giovannini, and C. Cappelli, "Multiple facets of modeling electronic absorption spectra of systems in solution," ACS Phys. Chem. Au **3**, 1–16 (2023).
[16]I.-M. Høyvik, B. Jansik, and P. Jørgensen, "Orbital localization using fourth central moment minimization," J. Chem. Phys. **137**, 224114 (2012).
[17]R. Z. Khaliullin, E. A. Cobar, R. C. Lochan, A. T. Bell, and M. Head-Gordon, "Unravelling the origin of intermolecular interactions using absolutely localized molecular orbitals," J. Phys. Chem. A **111**, 8753–8765 (2007).
[18]E. R. Sayfutyarova, Q. Sun, G. K.-L. Chan, and G. Knizia, "Automated construction of molecular active spaces from atomic valence orbitals," J. Chem. Theory Comput. **13**, 4063–4078 (2017).
[19]M. S. Gordon, D. G. Fedorov, S. R. Pruitt, and L. V. Slipchenko, "Fragmentation methods: A route to accurate calculations on large systems," Chem. Rev. **112**, 632–672 (2012).
[20]S. F. Boys, "Construction of some molecular orbitals to be approximately invariant for changes from one molecule to another," Rev. Mod. Phys. **32**, 296 (1960).
[21]J. Pipek and P. G. Mezey, "A fast intrinsic localization procedure applicable for *ab initio* and semiempirical linear combination of atomic orbital wave functions," J. Chem. Phys. **90**, 4916–4926 (1989).
[22]C. Edmiston and K. Ruedenberg, "Localized atomic and molecular orbitals," Rev. Mod. Phys. **35**, 457 (1963).
[23]J. W. Boughton and P. Pulay, "Comparison of the boys and Pipek–Mezey localizations in the local correlation approach and automatic virtual basis selection," J. Comput. Chem. **14**, 736–740 (1993).
[24]M. Sironi, A. Genoni, M. Civera, S. Pieraccini, and M. Ghitti, "Extremely localized molecular orbitals: Theory and applications," Theor. Chem. Acc. **117**, 685–698 (2007).
[25]F. Aquilante, T. Bondo Pedersen, A. Sánchez de Merás, and H. Koch, "Fast noniterative orbital localization for large molecules," J. Chem. Phys. **125**, 174101 (2006).
[26]T. Giovannini and H. Koch, "Energy-based molecular orbital localization in a specific spatial region," J. Chem. Theory Comput. **17**, 139–150 (2021).
[27]T. Giovannini and H. Koch, "Fragment localized molecular orbitals," J. Chem. Theory Comput. **18**, 4806–4813 (2022).
[28]Z. Li, H. Li, B. Suo, and W. Liu, "Localization of molecular orbitals: From fragments to molecule," Acc. Chem. Res. **47**, 2758–2767 (2014).
[29]H. Li, W. Liu, and B. Suo, "Localization of open-shell molecular orbitals via least change from fragments to molecule," J. Chem. Phys. **146**, 104104 (2017).
[30]B. Thapa, D. Beckett, K. Jovan Jose, and K. Raghavachari, "Assessment of fragmentation strategies for large proteins using the multilayer molecules-in-molecules approach," J. Chem. Theory Comput. **14**, 1383–1394 (2018).
[31]N. J. Mayhall and K. Raghavachari, "Molecules-in-molecules: An extrapolated fragment-based approach for accurate calculations on large molecules and materials," J. Chem. Theory Comput. **7**, 1336–1343 (2011).
[32]B. Thapa and K. Raghavachari, "Energy decomposition analysis of protein–ligand interactions using molecules-in-molecules fragmentation-based method," J. Chem. Inf. Model. **59**, 3474–3484 (2019).
[33]F. Wu, W. Liu, Y. Zhang, and Z. Li, "Linear-scaling time-dependent density functional theory based on the idea of 'from fragments to molecule,'" J. Chem. Theory Comput. **7**, 3643–3660 (2011).
[34]M. von Hopffgarten and G. Frenking, "Energy decomposition analysis," Wiley Interdiscip. Rev.: Comput. Mol. Sci. **2**, 43–62 (2012).
[35]L. Zhao, M. von Hopffgarten, D. M. Andrada, and G. Frenking, "Energy decomposition analysis," Wiley Interdiscip. Rev.: Comput. Mol. Sci. **8**, e1345 (2018).
[36]P. Su, Z. Tang, and W. Wu, "Generalized Kohn–Sham energy decomposition analysis and its applications," Wiley Interdiscip. Rev.: Comput. Mol. Sci. **10**, e1460 (2020).
[37]M. J. Phipps, T. Fox, C. S. Tautermann, and C.-K. Skylaris, "Energy decomposition analysis approaches and their evaluation on prototypical protein–drug interaction patterns," Chem. Soc. Rev. **44**, 3177–3211 (2015).
[38]Y. Mao, M. Loipersberger, P. R. Horn, A. Das, O. Demerdash, D. S. Levine, S. Prasad Veccham, T. Head-Gordon, and M. Head-Gordon, "From intermolecular interaction energies and observable shifts to component contributions and back again: A tale of variational energy decomposition analysis," Annu. Rev. Phys. Chem. **72**, 641–666 (2021).
[39]G. Bistoni, A. Altun, Z. Wang, and F. Neese, "Local energy decomposition analysis of London dispersion effects: From simple model dimers to complex biomolecular assemblies," Acc. Chem. Res. **57**, 1411 (2024).
[40]D. G. Fedorov and K. Kitaura, "Pair interaction energy decomposition analysis," J. Comput. Chem. **28**, 222–237 (2007).
[41]G. Bistoni, "Finding chemical concepts in the Hilbert space: Coupled cluster analyses of noncovalent interactions," Wiley Interdiscip. Rev.: Comput. Mol. Sci. **10**, e1442 (2020).
[42]E. D. Glendening and A. Streitwieser, "Natural energy decomposition analysis: An energy partitioning procedure for molecular interactions with application to weak hydrogen bonding, strong ionic, and moderate donor–acceptor interactions," J. Chem. Phys. **100**, 2900–2909 (1994).
[43]E. Pastorczak and C. Corminboeuf, "Perspective: Found in translation: Quantum chemical tools for grasping non-covalent interactions," J. Chem. Phys. **146**, 120901 (2017).
[44]C. D. Sherrill, "Energy component analysis of π interactions," Acc. Chem. Res. **46**, 1020–1028 (2013).
[45]R. M. Parrish, K. C. Thompson, and T. J. Martínez, "Large-scale functional group symmetry-adapted perturbation theory on graphical processing units," J. Chem. Theory Comput. **14**, 1737–1753 (2018).
[46]R. M. Parrish, D. F. Sitkoff, D. L. Cheney, and C. D. Sherrill, "The surprising importance of peptide bond contacts in drug–protein interactions," Chem. -Eur. J. **23**, 7887–7890 (2017).
[47]K. Kitaura and K. Morokuma, "A new energy decomposition scheme for molecular interactions within the Hartree–Fock approximation," Int. J. Quantum Chem. **10**, 325–340 (1976).
[48]W. J. Stevens and W. H. Fink, "Frozen fragment reduced variational space analysis of hydrogen bonding interactions. Application to the water dimer," Chem. Phys. Lett. **139**, 15–22 (1987).
[49]W. Chen and M. S. Gordon, "Energy decomposition analyses for many-body interaction and applications to water complexes," J. Phys. Chem. **100**, 14316–14328 (1996).
[50]P. S. Bagus and F. Illas, "Decomposition of the chemisorption bond by constrained variations: Order of the variations and construction of the variational spaces," J. Chem. Phys. **96**, 8962–8970 (1992).
[51]T. Ziegler and A. Rauk, "On the calculation of bonding energies by the Hartree Fock slater method: I. The transition state method," Theor. Chim. Acta **46**, 1–10 (1977).
[52]Y. Mo, J. Gao, and S. D. Peyerimhoff, "Energy decomposition analysis of intermolecular interactions using a block-localized wave function approach," J. Chem. Phys. **112**, 5530–5538 (2000).

[53]Y. Mo, P. Bao, and J. Gao, "Energy decomposition analysis based on a block-localized wavefunction and multistate density functional theory," Phys. Chem. Chem. Phys. **13**, 6760–6775 (2011).
[54]Q. Wu, P. W. Ayers, and Y. Zhang, "Density-based energy decomposition analysis for intermolecular interactions with variationally determined intermediate state energies," J. Chem. Phys. **131**, 164112 (2009).
[55]R. Cammi, R. Bonaccorsi, and J. Tomasi, "Counterpoise corrections to the interaction energy components in bimolecular complexes," Theor. Chim. Acta **68**, 271–283 (1985).
[56]B. Jeziorski, R. Moszynski, and K. Szalewicz, "Perturbation theory approach to intermolecular potential energy surfaces of van der Waals complexes," Chem. Rev. **94**, 1887–1930 (1994).
[57]K. Szalewicz, "Symmetry-adapted perturbation theory of intermolecular forces," Wiley Interdiscip. Rev.: Comput. Mol. Sci. **2**, 254–272 (2012).
[58]E. G. Hohenstein and C. D. Sherrill, "Wavefunction methods for noncovalent interactions," Wiley Interdiscip. Rev.: Comput. Mol. Sci. **2**, 304–326 (2012).
[59]G. Jansen, "Symmetry-adapted perturbation theory based on density functional theory for noncovalent interactions," Wiley Interdiscip. Rev.: Comput. Mol. Sci. **4**, 127–144 (2014).
[60]A. M. Pendás, M. Blanco, and E. Francisco, "Two-electron integrations in the quantum theory of atoms in molecules," J. Chem. Phys. **120**, 4581–4592 (2004).
[61]E. Francisco, A. Martín Pendás, and M. Blanco, "A molecular energy decomposition scheme for atoms in molecules," J. Chem. Theory Comput. **2**, 90–102 (2006).
[62]M. Blanco, A. Martín Pendás, and E. Francisco, "Interacting quantum atoms: A correlated energy decomposition scheme based on the quantum theory of atoms in molecules," J. Chem. Theory Comput. **1**, 1096–1109 (2005).
[63]T. M. Parker, L. A. Burns, R. M. Parrish, A. G. Ryno, and C. D. Sherrill, "Levels of symmetry adapted perturbation theory (SAPT). I. Efficiency and performance for interaction energies," J. Chem. Phys. **140**, 094106 (2014).
[64]W. B. Schneider, G. Bistoni, M. Sparta, M. Saitow, C. Riplinger, A. A. Auer, and F. Neese, "Decomposition of intermolecular interaction energies within the local pair natural orbital coupled cluster framework," J. Chem. Theory Comput. **12**, 4778–4792 (2016).
[65]A. Altun, M. Saitow, F. Neese, and G. Bistoni, "Local energy decomposition of open-shell molecular systems in the domain-based local pair natural orbital coupled cluster framework," J. Chem. Theory Comput. **15**, 1616–1632 (2019).
[66]A. Altun, R. Izsák, and G. Bistoni, "Local energy decomposition of coupled-cluster interaction energies: Interpretation, benchmarks, and comparison with symmetry-adapted perturbation theory," Int. J. Quantum Chem. **121**, e26339 (2021).
[67]A. Altun, F. Neese, and G. Bistoni, "Effect of electron correlation on intermolecular interactions: A pair natural orbitals coupled cluster based local energy decomposition study," J. Chem. Theory Comput. **15**, 215–228 (2018).
[68]P. Su and H. Li, "Energy decomposition analysis of covalent bonds and intermolecular interactions," J. Chem. Phys. **131**, 014102 (2009).
[69]P. Su, Z. Jiang, Z. Chen, and W. Wu, "Energy decomposition scheme based on the generalized Kohn–Sham scheme," J. Phys. Chem. A **118**, 2531–2542 (2014).
[70]P. Su, H. Liu, and W. Wu, "Free energy decomposition analysis of bonding and nonbonding interactions in solution," J. Chem. Phys. **137**, 034111 (2012).
[71]E. Caldeweyher, C. Bannwarth, and S. Grimme, "Extension of the D3 dispersion coefficient model," J. Chem. Phys. **147**, 034112 (2017).
[72]E. Caldeweyher, S. Ehlert, A. Hansen, H. Neugebauer, S. Spicher, C. Bannwarth, and S. Grimme, "A generally applicable atomic-charge dependent London dispersion correction," J. Chem. Phys. **150**, 154122 (2019).
[73]E. Caldeweyher, J.-M. Mewes, S. Ehlert, and S. Grimme, "Extension and evaluation of the D4 London-dispersion model for periodic systems," Phys. Chem. Chem. Phys. **22**, 8499–8512 (2020).
[74]A. Tkatchenko and M. Scheffler, "Accurate molecular van der Waals interactions from ground-state electron density and free-atom reference data," Phys. Rev. Lett. **102**, 073005 (2009).
[75]A. Tkatchenko, R. A. DiStasio, Jr., R. Car, and M. Scheffler, "Accurate and efficient method for many-body van der Waals interactions," Phys. Rev. Lett. **108**, 236402 (2012).
[76]O. A. Vydrov and T. Van Voorhis, "Nonlocal van der Waals density functional: The simpler the better," J. Chem. Phys. **133**, 244103 (2010).
[77]L. Goerigk and S. Grimme, "Double-hybrid density functionals," Wiley Interdiscip. Rev.: Comput. Mol. Sci. **4**, 576–600 (2014).
[78]R. Z. Khaliullin, A. T. Bell, and M. Head-Gordon, "Analysis of charge transfer effects in molecular complexes based on absolutely localized molecular orbitals," J. Chem. Phys. **128**, 184112 (2008).
[79]P. R. Horn, E. J. Sundstrom, T. A. Baker, and M. Head-Gordon, "Unrestricted absolutely localized molecular orbitals for energy decomposition analysis: Theory and applications to intermolecular interactions involving radicals," J. Chem. Phys. **138**, 134119 (2013).
[80]Y. Mao, P. R. Horn, and M. Head-Gordon, "Energy decomposition analysis in an adiabatic picture," Phys. Chem. Chem. Phys. **19**, 5944–5958 (2017).
[81]M. P. Mitoraj, A. Michalak, and T. Ziegler, "A combined charge and energy decomposition scheme for bond analysis," J. Chem. Theory Comput. **5**, 962–975 (2009).
[82]H. Shen and M. Head-Gordon, "Occupied-virtual orbitals for chemical valence with applications to charge transfer in energy decomposition analysis," J. Phys. Chem. A **128**, 5202–5211 (2024).
[83]J. Tomasi, B. Mennucci, and R. Cammi, "Quantum mechanical continuum solvation models," Chem. Rev. **105**, 2999–3094 (2005).
[84]B. Mennucci, "Polarizable continuum model," Wiley Interdiscip. Rev.: Comput. Mol. Sci. **2**, 386–404 (2012).
[85]*Continuum Solvation Models in Chemical Physics*, edited by B. Mennucci and R. Cammi (Wiley, New York, 2007).
[86]B. Mennucci, E. Cancès, and J. Tomasi, "Evaluation of solvent effects in isotropic and anisotropic dielectrics and in ionic solutions with a unified integral equation method: Theoretical bases, computational implementation, and numerical applications," J. Phys. Chem. B **101**, 10506–10517 (1997).
[87]J. Rezac and P. Hobza, "Describing noncovalent interactions beyond the common approximations: How accurate is the 'gold standard,' CCSD(T) at the complete basis set limit?," J. Chem. Theory Comput. **9**, 2151–2155 (2013).
[88]P. Jurečka, J. Šponer, J. Černý, and P. Hobza, "Benchmark database of accurate [MP2 and CCSD(T) complete basis set limit] interaction energies of small model complexes, DNA base pairs, and amino acid pairs," Phys. Chem. Chem. Phys. **8**, 1985–1993 (2006).
[89]J. Rezac and P. Hobza, "Advanced corrections of hydrogen bonding and dispersion for semiempirical quantum mechanical methods," J. Chem. Theory Comput. **8**, 141–151 (2012).
[90]A. Seidl, A. Görling, P. Vogl, J. A. Majewski, and M. Levy, "Generalized Kohn–Sham schemes and the band-gap problem," Phys. Rev. B **53**, 3764 (1996).
[91]R. Baer, E. Livshits, and U. Salzner, "Tuned range-separated hybrids in density functional theory," Annu. Rev. Phys. Chem. **61**, 85–109 (2010).
[92]J.-D. Chai and M. Head-Gordon, "Long-range corrected hybrid density functionals with damped atom–atom dispersion corrections," Phys. Chem. Chem. Phys. **10**, 6615–6620 (2008).
[93]T. Yanai, D. P. Tew, and N. C. Handy, "A new hybrid exchange–correlation functional using the Coulomb-attenuating method (CAM-B3LYP)," Chem. Phys. Lett. **393**, 51–57 (2004).
[94]M. A. Rohrdanz, K. M. Martins, and J. M. Herbert, "A long-range-corrected density functional that performs well for both ground-state properties and time-dependent density functional theory excitation energies, including charge-transfer excited states," J. Chem. Phys. **130**, 054112 (2009).
[95]R. H. Myhre and H. Koch, "The multilevel CC3 coupled cluster model," J. Chem. Phys. **145**, 044111 (2016).
[96]S. Sæther, T. Kjærgaard, H. Koch, and I.-M. Høyvik, "Density-based multilevel Hartree–Fock model," J. Chem. Theory Comput. **13**, 5282–5290 (2017).
[97]R. H. Myhre, A. M. Sánchez de Merás, and H. Koch, "Multi-level coupled cluster theory," J. Chem. Phys. **141**, 224105 (2014).

[98]S. D. Folkestad and H. Koch, "Equation-of-motion MLCCSD and CCSD-in-HF oscillator strengths and their application to core excitations," J. Chem. Theory Comput. **16**, 6869–6879 (2020).
[99]A. M. Sánchez de Merás, H. Koch, I. G. Cuesta, and L. Boman, "Cholesky decomposition-based definition of atomic subsystems in electronic structure calculations," J. Chem. Phys. **132**, 204105 (2010).
[100]G. Marrazzini, T. Giovannini, M. Scavino, F. Egidi, C. Cappelli, and H. Koch, "Multilevel density functional theory," J. Chem. Theory Comput. **17**, 791–803 (2021).
[101]T. Giovannini, G. Marrazzini, M. Scavino, H. Koch, and C. Cappelli, "Integrated multiscale multilevel approach to open shell molecular systems," J. Chem. Theory Comput. **19**, 1446–1456 (2023).
[102]T. Helgaker, P. Jorgensen, and J. Olsen, *Molecular Electronic-Structure Theory* (John Wiley & Sons, 2014).
[103]P. R. Horn, Y. Mao, and M. Head-Gordon, "Defining the contributions of permanent electrostatics, Pauli repulsion, and dispersion in density functional theory calculations of intermolecular interaction energies," J. Chem. Phys. **144**, 114107 (2016).
[104]F. Aquilante, L. Boman, J. Boström, H. Koch, R. Lindh, A. S. de Merás, and T. B. Pedersen, "Cholesky decomposition techniques in electronic structure theory," in *Linear-Scaling Techniques in Computational Chemistry and Physics* (Springer, 2011), pp. 301–343.
[105]H. Koch, A. Sánchez de Merás, and T. B. Pedersen, "Reduced scaling in electronic structure calculations using Cholesky decompositions," J. Chem. Phys. **118**, 9481–9484 (2003).
[106]O. Christiansen, P. Manninen, P. Jørgensen, and J. Olsen, "Coupled-cluster theory in a projected atomic orbital basis," J. Chem. Phys. **124**, 084103 (2006).
[107]I.-M. Høyvik, K. Kristensen, T. Kjærgaard, and P. Jørgensen, in *A Perspective on the Localizability of Hartree–Fock Orbitals*, edited by T. H. Dunning, Jr. (Springer, 2015), pp. 287–296.
[108]S. F. Boys and F. Bernardi, "The calculation of small molecular interactions by the differences of separate total energies. Some procedures with reduced errors," Mol. Phys. **19**, 553–566 (1970).
[109]P. R. Horn, Y. Mao, and M. Head-Gordon, "Probing non-covalent interactions with a second generation energy decomposition analysis using absolutely localized molecular orbitals," Phys. Chem. Chem. Phys. **18**, 23067–23079 (2016).
[110]P.-O. Löwdin, "On the nonorthogonality problem," in *Advances in Quantum Chemistry* (Elsevier, 1970), Vol. 5, pp. 185–199.
[111]K. E. Riley, J. Vondrášek, and P. Hobza, "Performance of the DFT-D method, paired with the PCM implicit solvation model, for the computation of interaction energies of solvated complexes of biological interest," Phys. Chem. Chem. Phys. **9**, 5555–5560 (2007).
[112]Y. Mao, M. Loipersberger, K. J. Kron, J. S. Derrick, C. J. Chang, S. M. Sharada, and M. Head-Gordon, "Consistent inclusion of continuum solvation in energy decomposition analysis: Theory and application to molecular CO_2 reduction catalysts," Chem. Sci. **12**, 1398–1414 (2021).
[113]D. Shen, P. Su, and W. Wu, "What kind of neutral halogen bonds can be modulated by solvent effects?," Phys. Chem. Chem. Phys. **20**, 26126–26139 (2018).
[114]S. D. Folkestad, E. F. Kjønstad, R. H. Myhre, J. H. Andersen, A. Balbi, S. Coriani, T. Giovannini, L. Goletto, T. S. Haugland, A. Hutcheson, I.-M. Høyvik, T. Moitra, A. C. Paul, M. Scavino, A. S. Skeidsvoll, Å. H. Tveten, H. Koch, "e^T 1.0: An open source electronic structure program with emphasis on coupled cluster and multilevel methods," J. Chem. Phys. **152**, 184103 (2020).
[115]J. C. Flick, D. Kosenkov, E. G. Hohenstein, C. D. Sherrill, and L. V. Slipchenko, "Accurate prediction of noncovalent interaction energies with the effective fragment potential method: Comparison of energy components to symmetry-adapted perturbation theory for the S22 test set," J. Chem. Theory Comput. **8**, 2835–2843 (2012).
[116]M. Pitoňák, K. E. Riley, P. Neogrády, and P. Hobza, "Highly accurate CCSD(T) and DFT–SAPT stabilization energies of H-bonded and stacked structures of the uracil dimer," ChemPhysChem **9**, 1636–1644 (2008).
[117]K. U. Lao, R. Schaffer, G. Jansen, and J. M. Herbert, "Accurate description of intermolecular interactions involving ions using symmetry-adapted perturbation theory," J. Chem. Theory Comput. **11**, 2473–2486 (2015).
[118]A. D. Becke, "Density-functional thermochemistry. III. The role of exact exchange," J. Chem. Phys. **98**, 5648–5652 (1993).
[119]P. Stephens, F. Devlin, C. Chabalowski, and M. J. Frisch, "Ab initio calculation of vibrational absorption and circular dichroism spectra using density functional force fields," J. Phys. Chem. **98**, 11623–11627 (1994).
[120]C. Adamo and V. Barone, "Exchange functionals with improved long-range behavior and adiabatic connection methods without adjustable parameters: The *m*PW and *m*PW1PW models," J. Chem. Phys. **108**, 664–675 (1998).
[121]R. M. Parrish, L. A. Burns, D. G. A. Smith, A. C. Simmonett, A. E. DePrince, E. G. Hohenstein, U. Bozkaya, A. Y. Sokolov, R. Di Remigio, R. M. Richard, J. F. Gonthier, A. M. James, H. R. McAlexander, A. Kumar, M. Saitow, X. Wang, B. P. Pritchard, P. Verma, H. F. Schaefer, K. Patkowski, R. A. King, E. F. Valeev, F. A. Evangelista, J. M. Turney, T. D. Crawford, and C. D. Sherrill, "Psi4 1.1: An open-source electronic structure program emphasizing automation, advanced libraries, and interoperability," J. Chem. Theory Comput. **13**, 3185–3197 (2017).
[122]D. G. A. Smith, L. A. Burns, A. C. Simmonett, R. M. Parrish, M. C. Schieber, R. Galvelis, P. Kraus, H. Kruse, R. Di Remigio, A. Alenaizan, A. M. James, S. Lehtola, J. P. Misiewicz, M. Scheurer, R. A. Shaw, J. B. Schriber, Y. Xie, Z. L. Glick, D. A. Sirianni, J. S. O'Brien, J. M. Waldrop, A. Kumar, E. G. Hohenstein, B. P. Pritchard, B. R. Brooks, H. F. Schaefer III, A. Y. Sokolov, K. Patkowski, A. E. DePrince III, U. Bozkaya, R. A. King, F. A. Evangelista, J. M. Turney, T. D. Crawford, C. D. Sherrill, T. D. Crawford, and C. D. Sherrill, "Psi4 1.4: Open-source software for high-throughput quantum chemistry," J. Chem. Phys. **152**, 184108 (2020).
[123]P. Linstrom (2017), NIST Chemistry WebBook—NIST Standard Reference Database Number 69, V.1.0, National Institute of Standards and Technology https://doi.org/10.18434/T4D303.
[124]R. Di Remigio, L. Frediani, and Contributors, *PCMSolver, an open-source library for the polarizable continuum model electrostatic problem*, http://pcmsolver.readthedocs.io/.
[125]R. Di Remigio, A. H. Steindal, K. Mozgawa, V. Weijo, H. Cao, and L. Frediani, "PCMSolver: An open-source library for solvation modeling," Int. J. Quantum Chem. **119**, e25685 (2019).
[126]A. K. Rappé, C. J. Casewit, K. Colwell, W. A. Goddard III, and W. M. Skiff, "UFF, a full periodic table force field for molecular mechanics and molecular dynamics simulations," J. Am. Chem. Soc. **114**, 10024–10035 (1992).
[127]S. Grimme, "Semiempirical GGA-type density functional constructed with a long-range dispersion correction," J. Comput. Chem. **27**, 1787–1799 (2006).
[128]A. Altun, F. Neese, and G. Bistoni, "Local energy decomposition analysis of hydrogen-bonded dimers within a domain-based pair natural orbital coupled cluster study," Beilstein J. Org. Chem. **14**, 919–929 (2018).
[129]L. A. Burns, M. S. Marshall, and C. D. Sherrill, "Comparing counterpoise-corrected, uncorrected, and averaged binding energies for benchmarking noncovalent interactions," J. Chem. Theory Comput. **10**, 49–57 (2014).
[130]R. M. Parrish, E. G. Hohenstein, and C. D. Sherrill, "Tractability gains in symmetry-adapted perturbation theory including coupled double excitations: CCD+ST(CCD) dispersion with natural orbital truncations," J. Chem. Phys. **139**, 174102 (2013).
[131]K. Patkowski, "Recent developments in symmetry-adapted perturbation theory," Wiley Interdiscip. Rev.: Comput. Mol. Sci. **10**, e1452 (2020).
[132]H. L. Williams and C. F. Chabalowski, "Using Kohn–Sham orbitals in symmetry-adapted perturbation theory to investigate intermolecular interactions," J. Phys. Chem. A **105**, 646–659 (2001).
[133]A. Heßelmann and G. Jansen, "First-order intermolecular interaction energies from Kohn–Sham orbitals," Chem. Phys. Lett. **357**, 464–470 (2002).
[134]A. Heßelmann and G. Jansen, "Intermolecular induction and exchange-induction energies from coupled-perturbed Kohn–Sham density functional theory," Chem. Phys. Lett. **362**, 319–325 (2002).
[135]A. Heßelmann and G. Jansen, "Intermolecular dispersion energies from time-dependent density functional theory," Chem. Phys. Lett. **367**, 778–784 (2003).
[136]A. J. Misquitta and K. Szalewicz, "Intermolecular forces from asymptotically corrected density functional description of monomers," Chem. Phys. Lett. **357**, 301–306 (2002).
[137]A. J. Misquitta, B. Jeziorski, and K. Szalewicz, "Dispersion energy from density-functional theory description of monomers," Phys. Rev. Lett. **91**, 033201 (2003).

[138]S. Grimme, S. Ehrlich, and L. Goerigk, "Effect of the damping function in dispersion corrected density functional theory," J. Comput. Chem. **32**, 1456–1465 (2011).
[139]M. S. Marshall, L. A. Burns, and C. D. Sherrill, "Basis set convergence of the coupled-cluster correction, δ(MP2)(CCSD(T)): Best practices for benchmarking non-covalent interactions and the attendant revision of the S22, NBC10, HBC6, and HSG databases," J. Chem. Phys. **135**, 194102 (2011).
[140]T. Giovannini and C. Cappelli, "Continuum *vs.* atomistic approaches to computational spectroscopy of solvated systems," Chem. Commun. **59**, 5644–5660 (2023).